MASARYKOVA UNIVERZITA
Přírodovědecká fakulta
Ústav teoretické fyziky a astrofyziky

Bakalářská práce

Brno 2023 Daniel Pitoňák

MASARYKOVA UNIVERZITA
PŘÍRODOVĚDECKÁ FAKULTA
ÚSTAV TEORETICKÉ FYZIKY A ASTROFYZIKY

OES spektrograf a jeho potenciál pro přesná měření radiálních rychlostí

Bakalářská práce

Daniel Pitoňák

Vedoucí práce: Dr. Petr Kabáth **Brno 2023**

Bibliografický záznam

Autor:	Daniel Pitoňák Přírodovědecká fakulta, Masarykova univerzita Ústav teoretické fyziky a astrofyziky
Název práce:	OES spektrograf a jeho potenciál pro přesná měření radiálních rychlostí
Studijní program:	B-FYZ Fyzika
Studijní obor:	ASTRO Astrofyzika
Vedoucí práce:	Dr. Petr Kabáth
Konzultant:	Raine Karjalainen, Ph.D
Akademický rok:	2022/2023
Počet stran:	$xiii + 53$
Klíčová slova:	OES; IRAF; Perkův dalekohled; Echelletová spektroskopie, Radiální rychlost hvězdy, Poměr signál/šum

Bibliographic Entry

Author:	Daniel Pitoňák Faculty of Science, Masaryk University Department of Theoretical Physics and Astrophysics
Title of Thesis:	The performance and the stability of the OES spectrograph
Degree Programme:	B-FYZ Physics
Field of Study:	ASTRO Astrophysics
Supervisor:	Dr. Petr Kabáth
Consultant:	Raine Karjalainen, Ph.D
Academic Year:	2022/2023
Number of Pages:	$xiii + 53$
Keywords:	OES; IRAF; Perek telescope; Echelle spectroscopy, Star radial velocity, Signal-to-noise ratio

Abstrakt

V této bakalářské práci se věnujeme efektivitě Ondřejovského Echelletového Spektrografu (OES) na Perkově dalekohledu. Roku 2019 zde proběhla rekonstrukce optické cesty. Původní systém zrcadel byl nahrazen novým optickým vláknem. Je nezbytné určit, jak velký vliv měla tato modernizace na kvalitu pozorování z hlediska propustnosti a spektroskopického výkonu. Tato práce si klade za cíl porovnat spektroskopická data získaná před a po rekonstrukci. Data získaná prostřednictvím OES byla zpracována programem IRAF. Porovnány byly hodnoty radiálních rychlostí vybraných hvězdných standardů a dále hodnoty poměru signálu a šumu. Tato práce shrne výkon nově rekonstruovaného dalekohledu a může být využita jako manuál k pozorování (výpočet potřebného expozičního času prostřednictvím ETC kalkulátoru) nebo jako podpora SW nástrojů pro pozorovatele. Práce vznikla v rámci projektu LTT-20015 (MŠMT).

Abstract

In this bachelor thesis I will present the efficiency of Ondřejov Echelle Spectrograph (OES) instrument at Perek telescope in Ondřejov. In 2019, the telescope's optical path was refurbished. The system of mirrors was replaced by new optical fibre. It is necessary to determine what effect this improvement had on the quality of the observations in terms of throughput and spectroscopic performance. The main goal of this bachelor thesis is comparison of the spectroscopic data obtained before and after the upgrade. Data collected by OES were processed by IRAF. For the comparison, I used radial velocity data of selected standard stars and values of signal to noise ratio. The thesis will summarize the performance of the newly refurbished telescope. Furthermore, this work can be also used as an observing manual with a new fiber mode (calculating of needed exposure time through ETC calculator) and eventually on SW tools to support the observer. Thesis was created as part of the project LTT-20015 (MŠMT).

MASARYKOVA UNIVERZITA
PŘÍRODOVĚDECKÁ FAKULTA
KOTLÁŘSKÁ 2, 611 37 BRNO
IČ: 00216224
DIČ: CZ00216224

ZADÁNÍ BAKALÁŘSKÉ PRÁCE

Akademický rok: 2022/2023

Ústav:	Ústav teoretické fyziky a astrofyziky
Student:	Daniel Pitoňák
Program:	Fyzika
Specializace:	Astrofyzika

Ředitel *ústavu* PřF MU Vám ve smyslu Studijního a zkušebního řádu MU určuje bakalářskou práci s názvem:

Název práce:	OES spektrograf a jeho potenciál pro přesná měření radiálních rychlostí
Název práce anglicky:	The performance and the stability of the OES spectrograph
Jazyk závěrečné práce:	angličtina

Oficiální zadání:
V této bakalářské práci se věnujeme efektivitě Ondřejovského Echelletového Spektrografu (OES) na Perkově dalekohledu. Roku 2019 zde proběhla rekonstrukce optické cesty. Původní systém zrcadel byl nahrazen novým optickým vláknem. Hlavním cílem práce je určení vlivu modernizace na kvalitu pozorování z hlediska propustnosti a spektroskopického výkonu. Dílčí cíle: Student v rámci práce zpracuje a analyzuje spektroskopická data ze spektrografu OES, která byla pořízena před a po modernizaci a porovná parametry jako Signal-to-noise ratio a další ukazatele kvality dat. Cílem je také zjištění vlivu parametrů jako vzdušná hmota a citlivost detektoru v různých vlnových délkách. Posledními dvěma výstupy bude monitorování a srovnání přesnosti stadardní hvězdy pro určování radiálních rychlostí a pak vypracování návrhu Exposure time kalkulátoru, který v budoucnu umožní lepší odhad potřebné doby pro OES.

Literatura:
KABÁTH, Petr, Marek SKARKA, S. SABOTTA, E. GUENTHER, David JONES, T. KLOCOVÁ, J. ŠUBJAK, Jiří ŽÁK, Magdalena ŠPOKOVÁ, Martin BLAŽEK, J. DVOŘÁKOVÁ, D. DUPKALA, J. FUCHS, A. HATZES, E. KORTUSOVÁ, R. NOVOTNÝ, E. PLÁVALOVÁ, L. ŘEZBA, J. SLOUP, P. ŠKODA a M. ŠLECHTA. Ondřejov echelle spectrograph, ground based support facility for exoplanet missions. *Publications of the Astronomical Society of the Pacific*. Bristol: IOP Publishing Ltd., 2020, roč. 132, č. 1009, s. 1-12. ISSN 0004-6280. doi:10.1088/1538-3873/ab6752.

Vedoucí práce:	Bc. Petr Kabáth, Dr. rer. nat.
Konzultant:	Raine Karjalainen, Ph.D.
Datum zadání práce:	15. 9. 2022
V Brně dne:	21. 5. 2023

Zadání bylo schváleno prostřednictvím IS MU.

Daniel Pitoňák, 18. 5. 2023
Bc. Petr Kabáth, Dr. rer. nat., 18. 5. 2023
RNDr. Luboš Poláček, 18. 5. 2023

Poděkování

Na tomto místě chci poděkovat vedoucímu práce Dr. Petru Kabáthovi a konzultantu Rainemu Karjalainemu, Ph.D., za jejich vedení a trpělivost. Je na místě poděkovat i pozorovatelům z ondřejovského Stelárního oddělení Astronomického ústavu Akademie věd České republiky za nafocení spekter, která byla v této práci použita. Za pomoc s angličtinou a překladem textů děkuji Pavlíně Češkové a Janě Banášové. Spolužákům z ročníku děkuji za četné cenné rady a v neposlední řadě děkuji samozřejmě i mé rodině.

Prohlášení

Prohlašuji, že jsem svoji bakalářskou práci vypracoval samostatně pod vedením vedoucího práce s využitím informačních zdrojů, které jsou v práci citovány.

Brno 23. května 2023 . . . . . .

Daniel Pitoňák

Contents

Used acronyms ..... **xiii**

Introduction **1**

Chapter 1. Measurement methods **3**
1.1 Star's radial velocity 3
1.1.1 Spectroscopy 4
1.1.2 Doppler effect 7
1.2 Signal-to-noise ratio 9

Chapter 2. Instruments description **11**
2.1 The Perek telescope 11
2.1.1 Location and conditions 12
2.1.2 History of the telescope 12
2.2 Ondřejov Echelle Spectrograph 13
2.3 Modernization in 2019 15

Chapter 3. Observation and data processing **21**
3.1 Observed stars 21
3.2 Observations 21
3.3 Data processing 23
3.3.1 RV measurement 24
3.3.2 SNR measurement 26

Chapter 4. Results **29**
4.1 RV results 29
4.2 SNR results 30
4.2.1 Long-term data sets and SNR 30
4.2.2 Influence of the air mass on the SNR 32
4.2.3 Exposure time calculator and the SNR 32
4.2.4 Theoretical values of RV uncertainties 36

Conclusion **37**

Appendix **39**

A Parameters of the fibre cable 39
B Parameters of the CCD camera 41
C Scripts for RV measurement 43

References 49

Used acronyms

I attached a table of used acronyms for easier orientation in the text.

ETC	exposure time calculator
FWHM	full width at half maximum
IRAF	Image Reduction and Analysis Facility
OES	Ondřejov Echelle Spectrograph
RV	radial velocity
SNR	signal-to-noise ratio
Th-Ar	thorium-argon

Introduction

The Perek telescope, located in Ondřejov near Prague, is the biggest telescope which works in the Czech Republic. It is also the biggest telescope that was ever constructed on the territory of the former Czechoslovakia. Nowadays, the telescope is used by the Department of Stellar Physics of the Astronomical Institute of the Czech Academy of Sciences for exoplanetary research. Work is focused especially on the confirmation of the exoplanetary candidates. In 2019, the telescope's optical path was refurbished. Until 2019, caught light was guided by a system of mirrors. This system was newly replaced by fibre optics.

How did the telescope's efficiency change after this upgrade? Has it increased or is it still as similar as it was before the upgrade? How does the efficiency of different wavelengths differ from each other? This thesis will try to answer these questions.

In the first chapter, I will describe the theory hidden behind the measurement of radial velocities which is the main scientific task of the Ondřejov Echelle Spectrograph instrument. In this paper, I measure the efficiency of the telescope in two ways: radial velocity and signal-to-noise. Both will be described in the first chapter. Secondly, I will continue with the description of the instruments. Information about the Perek telescope, Ondřejov Echelle Spectrograph, or improvement which was done in 2019 will be discussed in the second chapter. The third chapter describes the targets, selected observations and data processing. Here we will look at how data were chosen and how were data processed. The next chapter describes the results of data processing. Our goal is to compare the measured radial velocities of the standard star and the calculated signal-to-noise ratios. This part includes an exposure time calculator which can be used by observers for increasing the efficiency of their observations. The last part will conclude the whole work.

Chapter 1

Measurement methods

Our task is to find out how was the telescope's ability to measure the needed parameters of the observed stars changed after the improvement of its optical path. For this reason, we selected two ways to describe any changes. The first one uses the measuring radial velocities. We expect decreasing in the variance of results. The second way follows the signal-to-noise ratio. This value should increase after improvement. We will observe these quantities and watch how did upgrade affect them.

First of all, we have to describe all physical phenomena related to our work and define physical quantities which we will measure and compare.

1.1 Star's radial velocity

As everybody knows, stars are not motionless objects of the night sky. After long observations, we can notice stars are slowly changing their positions in view of the surrounding starry background. As you can see in Figure 1.1, the direction of the star's motion in space can be spread in two directions: transverse velocity and radial velocity.

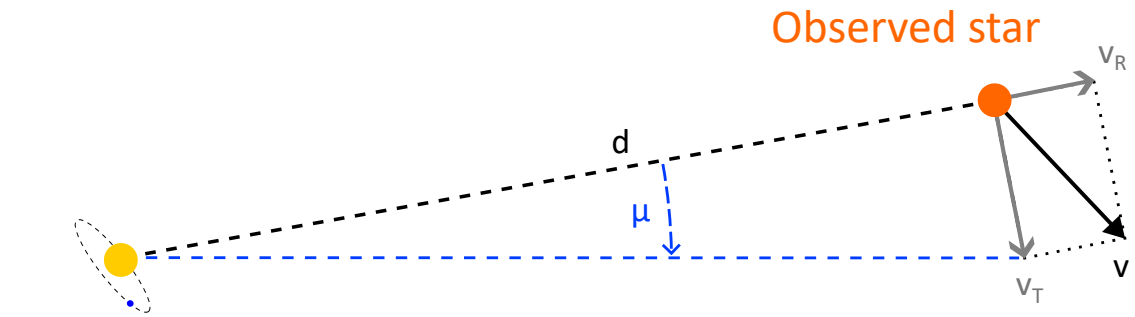

Figure 1.1: Diagram of star's motion - Distance d separates our Solar system and observed star. The star is moving at speed v. Transverse velocity is observable from Earth by proper motion μ on the night sky. Radial velocity v_R has an effect on distance. Inspired by Wikipedia picture.

Transverse velocity is responsible for the proper motion of the star. This motion can be observed in the night sky usually after a long time. The observed star is simply changing

its position in view of surrounding stars. The highest value of the proper motion was measured at the very known Barnard's Star, located in the constellation of Ophiuchus. This value is 10.4 arcseconds per year (Gaia Collaboration et al., 2022).

On the other hand, radial velocity is responsible for changes in the distance between the observed object and our Sun. That means this part of the star's motion is not visually noticeable by changing the star's position in the night sky. The way to observe and then measure radial velocity is hidden in the light travelling from the observed object.

1.1.1 Spectroscopy

For now, we have to go back to the start of the light's journey – directly to the observed star. Light is somehow affected by the stellar atmosphere where it starts its journey. Spectroscopy which is describing this physical phenomenon began to be discovered more than 300 years ago.

The beginnings of spectroscopy started in 1648 with a physical description of the principle of a rainbow by Bohemian doctor and scientist Jan Marek Marci. He confirmed his theory about the refraction of beams by experimenting with the dispersion of light on the prism. However, Jan Marek Marci was not the only one who did experiments with the refraction of light at the same time. Similar experiments were done by Athanasius Kircher (1646), Robert Boyle (1664), and Francesco Maria Grimaldi (1665), but today the most famous is Sir Isaac Newton (Burgess, 1987). He observed the dispersion of light in 1666 and after a few years later he united dispersed light back into the white beam (MIT Spectroscopy). Moreover, he remarked that the more monochromatic light he refracted, the lower intensity this light has (Ball, 1908).

In 1800, William Herschel discovered infrared radiation through his experiment with a glass prism and thermometer. Until this discovery, nobody knew about invisible parts of the light spectrum (Williams, 2002). The ultraviolet part was first observed by Johann Wilhelm Ritter one year after Herschel's discovery, in 1801. He used a silver chloride-soaked paper in the blue end of the visible spectrum and found out that violet visible light is not darkening paper as much as it darkened the area behind the visible part (Hockberger, 2002).

In 1802, William Hyde Wollaston observed dark lines in the spectrum of the Sun's light and believed that these dark lines represent boundaries between colours (Wollaston, 1802). This explanation was dispelled by Joseph von Fraunhofer (OpenStax Astronomy, 2016). In 1814, he started systematically writing down all visible dark lines in the Sun's spectrum. He was the first one who used a diffraction grating in his work with refraction light (Brand, 1995). Throughout his life, he catalogued over 570 spectral lines which were named after Fraunhofer (Fraunhofer, 1815). In Figure 1.2, you can see the most obvious Fraunhofer lines.

It was known for a long time that chemical substances affect light. For example, already in the 17th century was known that distinct colours will appear after adding salts to alcohol flames (Talbot, 1826). In 1849, J. B. L. Foucault described that absorption and emission lines of the same chemical element can be found at the same wavelength. The only difference between these two situations is in the temperature of the light source (Brand, 1995). The same idea was independently predicted by A. J. Ångström, but 4 years

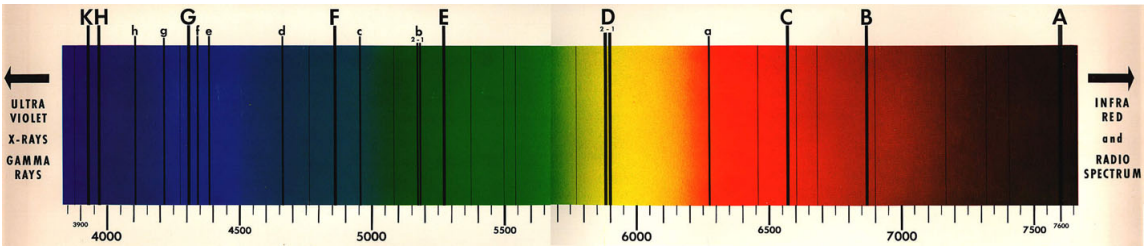

Figure 1.2: Fraunhofer lines in the visible light spectrum - The most obvious Fraunhofer lines are marked with printing letters. Some of them are very common, e. g. C line is notorious Hα or D lines are sodium doublet. Credit: website of Columbia Edu

after Foucault, in 1853 (Ångström, 1853). The specific relation between a source of light and its spectral lines was defined by Robert Bunsen and Gustav Kirchhoff during the 1860s. They identified Fraunhofer lines in the spectrum of light emitted by laboratory source (Bunsen & Kirchhoff, 1861). During their work, they laid the foundations of analytical spectroscopy and with its help discovered two new chemical elements - caesium and rubidium (Weeks, 1956). The differences between emission and absorption spectral lines are characterized by three laws of spectroscopy:

> *We are now can summarize the formation of spectra with three rules known as Kirchhoff's laws, from Gustav Kirchhoff (1824-1887): see Figure 2.5.*
>
> 1. *An incandescent solid or opaque gas under high pressure will produce a continuous spectrum.*
> 2. *A low-density gas will radiate an emission-line spectrum (with an underlying emission continuum).*
> 3. *Continuous radiation viewed through a low-density gas will produce an absorption-line spectrum (with an associated absorption continuum). And the absorptions will be inverses of the emissions.*
>
> (James B. Kaler, Stars and their spectra, 2011)

The figure reference included in the quote is valid of course only in the book itself. Figure illustrating these three situations is numbered 1.3 in this work.

Discoveries of other parts of the electromagnetic spectrum followed. Wilhelm Conrad Roentgen uncovered X-rays as part of the electromagnetic spectrum in 1895 and one year later Antoine Henri Becquerel continued with the detection of radioactivity (Novelline, 1987; Berkeley Lab, 2000).

In the 20th century, it opened a completely new perspective on some physical problems. For example, the photoelectric effect was first observed by Heinrich Hertz in 1887 (Hertz, 1887). The explanation of this phenomenon came from Einstein in 1905 when he published his work with a prediction of light being composed of numerous parts - today known as photons. Each photon is the carrier of a certain part of an energy - quantum (Einstein, 1905). This idea was confirmed in 1919 by the same physical phenomenon. Experiments with the photoelectric effect were realized by Robert Millikan and Einstein was awarded the Nobel Prize in 1921 (Millikan, 1914; Nobelpreize.org, 1921).

Figure 1.3: Diagram of Kirchhoff laws - Inspired by Palma.

One of the biggest steps in the field of spectroscopy was publishing the Bohr model of the atom in 1913. This model assumes a massive atomic nucleus of protons and neutrons and an electron shell composed of electron orbits. Each orbit is specific by its energy which describes Equation 1.1 where we can find mass m and charge e of an electron, vacuum permittivity ε_0, reduced Planck constant $\hbar$ and a quantum number of equivalent energy level n (Bohr, 1913).

$$E_\mathrm{n} = -\frac{me^4}{2(4\pi\varepsilon_0)^2\hbar^2} \cdot \frac{1}{n^2} \tag{1.1}$$

Electrons can "travel" between these levels depending on the energy of absorbed or emitted photons. This model allows us to describe the creation of hydrogen spectral lines and their series (most known are the Lyman, the Balmer, and the Paschen series). If a photon is to interact with the electron shell, it must have a precise dose of energy E_p that corresponds with the energy difference between two arbitrary energy levels, as you can see in Equations 1.2 and 1.3. In this case, we assume orbits m and n where $m > n$.

$$E_\mathrm{p} = E_\mathrm{m} - E_\mathrm{n} \tag{1.2}$$

$$E_\mathrm{p} = \frac{me^4}{2(4\pi\varepsilon_0)^2\hbar^2}\left(\frac{1}{n^2} - \frac{1}{m^2}\right) \tag{1.3}$$

Photon can be absorbed only in this case and electrons will get to a higher energy level. The process can also be reversed. However, the emitted photon will have an energy that again corresponds to the difference in energy levels between which the electron moved. Both situations (photon absorption and emissions) are depicted in Figure 1.4. Each atom has unique series of electron orbits and thus also a series of spectral lines. This is why spectral lines are something like fingerprints of the chemical elements. Light carries a large amount of information about the content of a star's atmosphere. It is clear from practice that if we will examine star's spectra, we will not usually find most of the spectral lines on their known positions. The shift between the observed spectral line wavelength and the laboratory-measured value of the wavelength of the same spectral line is connected with the motion of the observed star. This influence of movement on emitted waves is known as the Doppler effect.

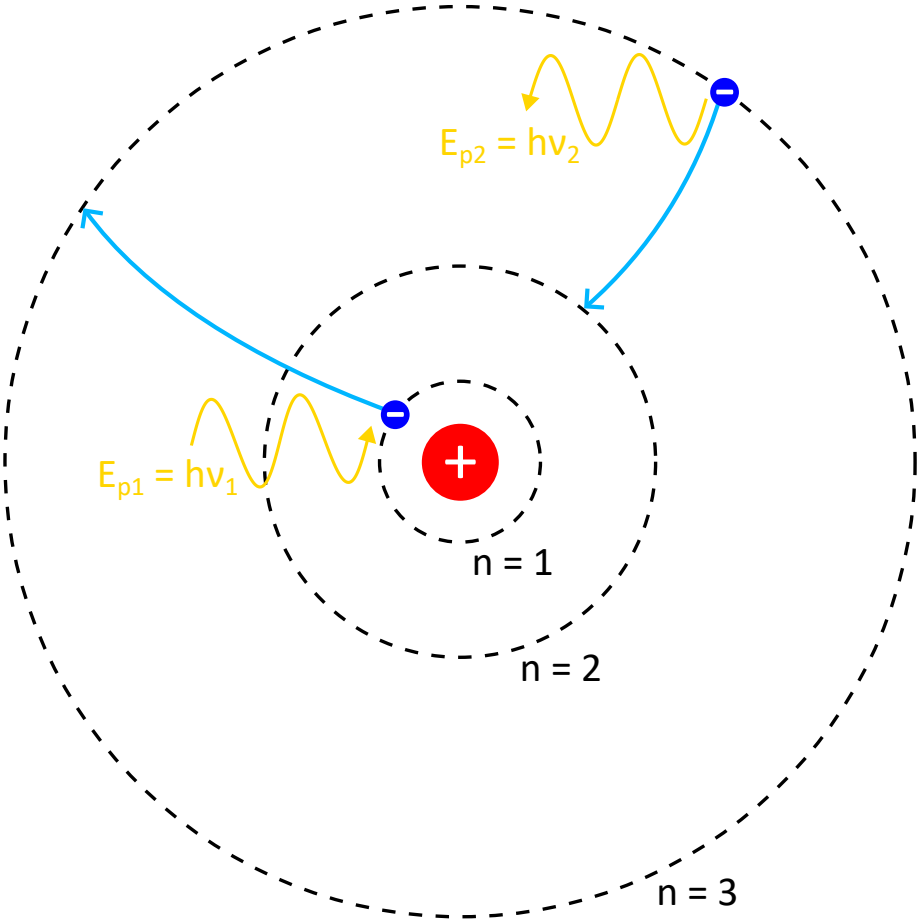

Figure 1.4: Diagram of Bohr model of the atom - Inspired by Wikipedia picture.

1.1.2 Doppler effect

All of us know that sound. The sound of a passing car, ambulance, train, etc. However, the sound is an inappropriate word for this physical phenomenon. A better description is sound's change because we can really hear changes in the tone depending on the direction and velocity of the sound's source. The first one who discovered this phenomenon and after whom is this phenomenon named was Christian Doppler. He predicted this phenomenon in 1842 after his work on binary stars (Eden, 1992). Buys Ballot, today more known for his work in the field of meteorology, refused to believe the validity of Doppler's theory. Therefore he arranged an experiment with a moving train and a group of musicians on its board in 1845. The experiment did not show the expected result. The tone was higher during the train's arrival and after passing tone decreased under the emitted one. This confirmed Doppler's theory (Utrecht University, 2023). After 3 years, in 1848, the same phenomenon was discovered for electromagnetic waves by French physicist Hippolyte Fizeau (Houdas, 1991). Nowadays, we can find many applications of the Doppler effect. For example, measuring the velocity of cars by police, describing blood flow in medicine - Doppler ultrasonography, in fluid flow measurement by laser, in the cosmos for communication with very fast satellites, and last but not least in astronomy (Wikipedia, 2023).

Doppler effect can be generally described by Equation 1.4. This equation includes not only the motion of the source but also the motion of the observer (detector).

$$f = \left(\frac{v + v_D}{v + v_S}\right) f_0 \tag{1.4}$$

All needed physical quantities are listed in Table 1.1.

Symbol	Physical quantity
f	observed frequency
f_0	emitted frequency
v	velocity of wave propagation
v_D	detector velocity
v_S	source velocity

Table 1.1: Definition of physical quantities in the Equation 1.4

In this equation, it is necessary to follow generally accepted velocity direction notation. The positive velocity of the observed source $+v_S$ is understood as motion away from the detector. Waves are getting longer than emitted ones and thus redshift is created. On the contrary, the source's negative velocity $-v_S$ is measured if the source is getting closer to the detector. Observed waves are shorter than emitted ones. This is known as blueshift. Notation is depicted in Figure 1.5.

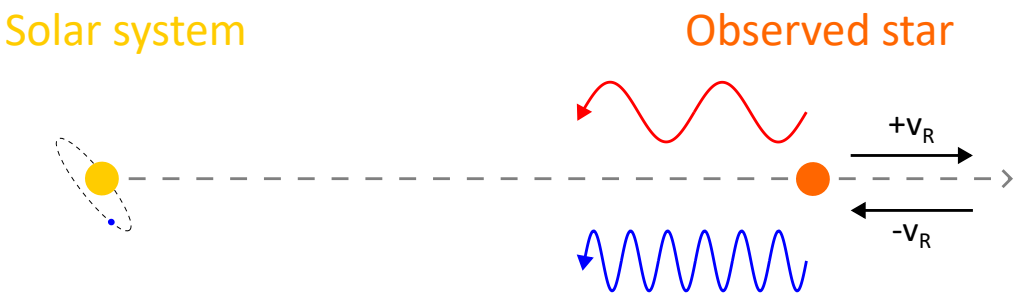

Figure 1.5: Motion of the observed star and its influence on emitted wave

Equation 1.4 is for our purpose very general. We can modify the equation for measuring a star's radial velocity. We are interested in the motion of the observed star relative to us. That means we can consider the detector (the Solar system) as motionless $v_S = 0$. Then the velocity of the source (star) is radial velocity v_R. Also, we know the velocity of the wave propagation in the vacuum, it is the speed of light c. Now, we can rewrite Equation 1.4 and the result is Equation 1.5.

$$f = \frac{c}{c + v_R} f_0 \tag{1.5}$$

Electromagnetic waves can be described by two physical quantities: wavelength λ or frequency f. Both are equivalent so it does not matter which one is used. Spectrograph creates an electromagnetic spectrum as a line. It is more intuitive to work with wavelength. Therefore, we have to use relation 1.6 between frequency and wavelength. Further, we can observe on the one-line spectrum that spectral lines are shifted by the Doppler effect. This shift is defined as the difference 1.7 between observed wavelength λ and emitted wavelength λ_0. In combination with Equation 1.5 and after several equation adjustments we can get relation 1.8 for radial velocity v_R.

$$f = \frac{c}{\lambda} \tag{1.6}$$

$$\Delta\lambda = \lambda - \lambda_0 \tag{1.7}$$

$$v_\mathrm{R} = \frac{\Delta\lambda}{\lambda_0} c \tag{1.8}$$

Telescope's upgrade should affect the difference in the measured star's radial velocities values. This method will compare velocities measured before and after the telescope's improvement.

1.2 Signal-to-noise ratio

The signal-to-noise ratio is a dimensionless quantity describing the quality of electromagnetic wave observation. In Figure 1.6 we can see the noise is a random undesirable signal, which is unfortunately unavoidable. Noise can be caused in many ways mentioned below. A stable signal can be in the plot illustrated as a high peak and SNR describes how dominant and recognizable is this peak. SNR can be simply characterized as a proportion of signal power P_S to the power of noise P_N, as you can see in Equation 1.9.

$$SNR = \frac{P_\mathrm{S}}{P_\mathrm{N}} \tag{1.9}$$

Equation 1.9 is describing the quality of whatever signal: acoustic, radio, or optical. However, this equation is for our use very general so we will use the relation between SNR and exposure time of the image. According to Massey & Jacoby (1992), this relation can be written in the form 1.10.

$$SNR = \frac{N \times t}{\sqrt{N \times t + S \times p \times t + p \times R^2}} \tag{1.10}$$

There are several quantities: N is a count rate from the star and t is exposure time. The denominator of the fraction includes three parts such as a photon noise of the star, a photon noise of the sky, and a read-noise of the device. The photon noise is defined by the count rate N and exposure time t. The photon noise of the sky includes count rate per pixel S, number of used pixels in measured aperture n, and again exposure time t. The last term of the equation describes the read-noise of the device which additionally contains the read-noise per pixel R.

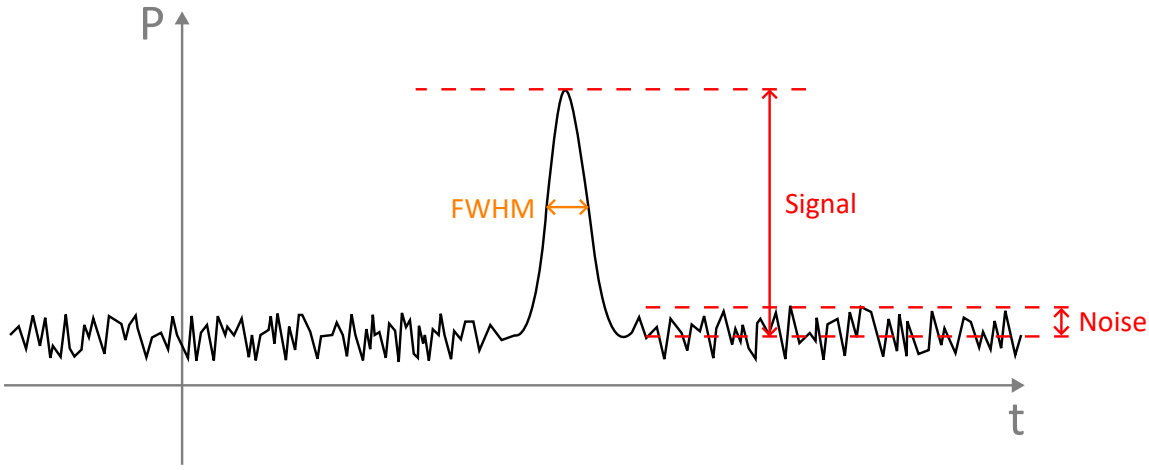

Figure 1.6: Diagram of an observed signal and noise - Inspired by Shimadzu Corporation.

If we assume that the signal can be described by Gaussian distribution then it is possible to calculate SNR from statistical parameters of the Gaussian peak. This relation is shown in Equation 1.11.

$$SNR = \sqrt{1.06 \times (Counts - Bias) \times FWHM \times Gain} \tag{1.11}$$

The relation includes a number of overall measured counts of the signal $Counts$, value of the background $Bias$, full width at half maximum $FWHM$, and set gain of the CCD chip $Gain$.

According to Gustafsson (1992), knowledge of SNR and spectrograph characteristic parameters enable the calculation of theoretical uncertainty of RV measurement. This relation is described in Equation 1.12.

$$\sigma_{\mathrm{RV}} = C \times (SNR)^{-1} \times \Delta\lambda^{-0.5} \times R^{-1.5} \tag{1.12}$$

It occurs in this equation instrument specific constant C, signal-to-noise ratio SNR, observed wavelength range $\Delta\lambda$, and resolving power R.

Chapter 2

Instruments description

2.1 The Perek telescope

The Perek telescope is a reflecting telescope located in the observatory area of the Astronomical Institute of The Czech Academy of Sciences in Ondřejov near Prague. The telescope is with its 2 meters diameter large parabolic primary mirror today the biggest optical instrument in the Czech Republic. Since 2012, it has been named after Luboš Perek (1919-2020) who participated in the telescope's establishment (Trnka, 2012). Nowadays, this facility is available for researchers from all Czech institutions, especially students from the Faculty of Mathematics and Physics of Charles University in Prague and from the Faculty of Science of Masaryk University in Brno. Telescope is equipped with a single-order spectrograph and echelle spectrograph (known as Ondřejov Echelle Spectrograph - OES). The whole facility is hidden under a large dome with a diameter of 21 meters (website of the Stellar department, 2023).

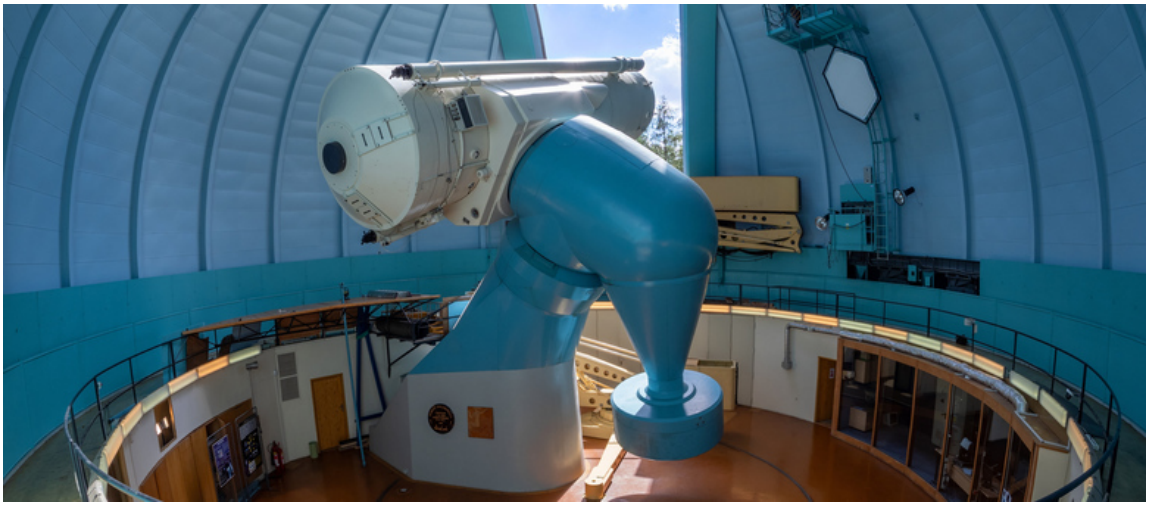

Figure 2.1: The Perek telescope - Credit: website of the Stellar department

2.1.1 Location and conditions

The location of the telescope is about 30 kilometres southeast of Prague. The area of the Astronomical Institute is spread in the north part of the Ondřejov, a village with 1 800 inhabitants (Wikipedia - Ondřejov, 2023). Telescope itself is located in the northern part of the observatory, approximately 600 meters away from the observatory's historical part. It stands on the slope of Pecný hill at an altitude of 528 meters above sea level (website Parameters of the Perek telescope, 2023). We can find there several buildings of the astronomical observatory, one optical telescope with a diameter of 65 centimetres, one sun radiotelescope with a diameter of 10 meters, and on the top of Pecný hill (545 meters above sea level) is located geodetic observatory of The Research Institute of Geodesy, Topography and Cartography (Wikipedia - Pecný, 2023). By the driveway, there are temporarily located two Cherenkov telescopes in test mode before their journey to Chile. Climate and landscape are typical for central Europe. The closest surroundings are forested. According to Kabáth et al. (2020), observation by the Perek telescope is possible only if the Sun is 12° below the horizon. Times of sunsets and sunrises depend on the season. In December 2015 were 372 observable hours, on the other hand in June 2015 was observation possible only during 84 hours. However, the real number of observed hours is strongly affected by weather. Statistically speaking, conditions for observing are bad during the winter period due to high humidity and low-level clouds. The proportion of observed hours to all observable hours is higher in the summer, around 30 and 40 % from March to September. Between October and February, it is only a few percent. Useful data can be collected during 25-30 % of all available observing time of the whole year. Ordinary seeing in Ondřejov is from $2''$ to $3''$, but excellent conditions provide seeing $1.5''$.

2.1.2 History of the telescope

Building of the telescope's facility started in 1963 and the telescope was commissioned in 1967 on the occasion of the 13th congress of the International Astronomical Union. Telescope itself was constructed by Carl Zeiss Jena as a twin telescope of the Alfred Jensch telescope in Tautenburg (near Jena) in Germany. Moreover, this company has made very similar facilities in Shamakhy (Azerbaijan), Rozhen (Bulgaria), and in Terskol (Russia). However, the telescope in Ondřejov was designed to be universal. All three foci (primary, Cassegrein, and Coudé) were equipped with spectrographs. Only primary and Cassegrain foci had cameras for direct photography. All these instruments were recorded on photographic glass plates. The size of glass plates used with cameras for direct photographing was 59×59. Parameters of plates used with spectrographs are mentioned in Table 2.1. This combination of devices allowed observing objects with different brightness. Less bright objects were projected in primary focus and very bright objects were projected in Coudé focus (Šlechta, 2020).

Over the years the facility was modernized. In the 80s the control system was changed. The original one was changed to one developed by the Hungarian company VILATI. Between the years 1996 and 1998, a new system by Science Systems company was installed. In 2006 was improved the control electronics of the telescope and in 2009 was changed the control electronics of spectrographs. Both were made by ProjectSoft HK. Recording media has changed over the years. The first electronic detector Reticon was borrowed

	Primary focus	Cassegrein focus	Coudé focus
Size [mm]	11×50	12.5×60 19.5×126	9×120 13.3×226 18.5×385
Resolution [Å/mm]	33–400	10–75	4.3–34.4

Table 2.1: Table of the glass plates sizes and their resolutions - Credit: Šlechta (2020)

from The Lick Observatory and installed in 1992. Only since 1997, CCD chips cooled by liquid nitrogen have been permanently used. A new echelle spectrograph was built in 2004. It is described in the following part of this chapter (Šlechta, 2020).

2.2 Ondřejov Echelle Spectrograph

An echelle spectrograph is one construction type of spectrograph. The common spectrograph contains prism or diffraction grating which creates a long one-line spectrum from the observed star. This spectrum allows us to measure the equivalent width of spectral lines such as H or He lines of hot stars. This value is necessary for finding out the physical properties of the observed star. On the other hand, the echelle spectrograph contains echelle grating which creates parallel parts of the original spectrum. The final image resembles the ladder. That is why it is called "echelle spectrograph" because "echelle" means in French "ladder". Spectrum is more accurate and usually is used for measuring a star's RV (Šlechta, 2020).

OES is located on the ground floor of the telescope's building in temperature stabilized Coudé room. The optical path from the telescope leads to the Coudé room. The arrangement of the spectrograph is captured in Figure 2.2.

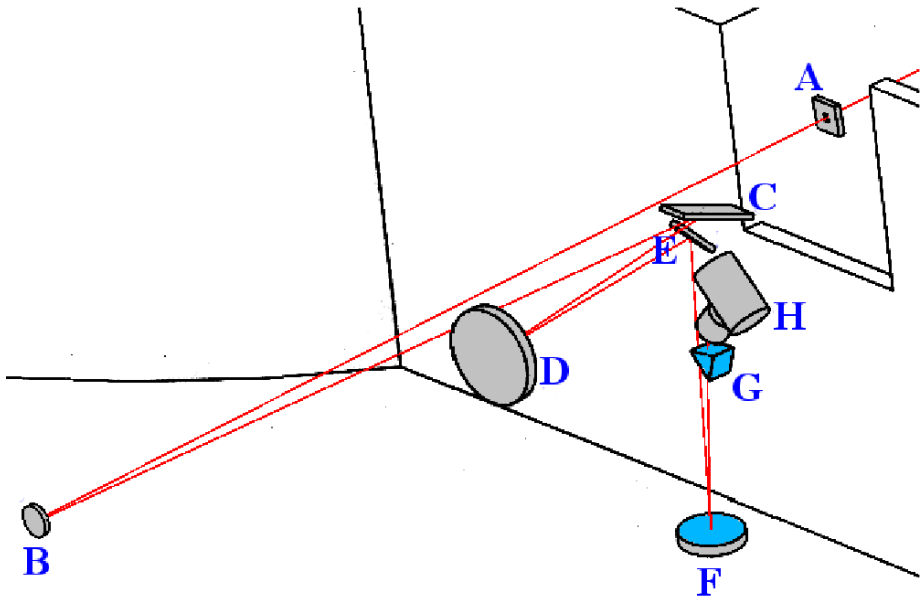

Figure 2.2: Scheme of the OES - Credit: website about OES

Light is coming from the slit (A) which is responsible for image sharpness and shielding off-axis beams (Miroslav Šlechta, 2023). From the slit, the light continues to the collimator (B). The next part is echelle grating (C - Figure 2.3). From there, light is directed to the white pupil section which narrows the light beam. This section contains the first parabolic mirror (D), the plane mirror (E), and the second parabolic mirror (F). Before recording light beam is dispersed by the glass prism (G) and separated orders are shown in the CCD camera (H) cooled by Dewar. The chip is cooled to the temperature around $-110\,°\mathrm{C}$. Technical details are listed in Tables 2.2 and 2.3. More detailed information can be found in Koubský et al. (2004) and on website about OES (2023).

Label	Component	Focal ratio	Focal length [mm]
B	collimator	f/32	4637
D	first parabolic mirror	f/3.6	1628
E	flat mirror	-	-
F	secondary parabolic mirror	f/3.1	1086

Table 2.2: Specifications of mirrors used in OES - Credit: Koubský et al. (2004)

Label	Component	Notes	Model
A	slit	width 0.6 mm	-
C	echelle grating	157×412 mm grating 54.5 g/mm blaze angle $\theta = 69°$	Richardson Grating Laboratories
G	prism	$114 \times 118 \times 140$ mm diffraction angle 54.5° material Schott LF5 density 3.25 $\mathrm{g/m^3}$	Walter, Faculty of Mathematics and Physics, Charles University in Prague
H	camera lens	f/1.8, f = 200 mm	CANON EF 200
-	CCD camera	chip EEV 42-40-1-368 resolution 2048×2048 pixel size 13.5 µm	VersArray 2048B, Roper Scientific

Table 2.3: Specifications of other components used in OES - Credits: website about OES (2023); Koubský et al. (2004)

According to Kabáth et al. (2020), OES was able to create an image of a $V_{mag} = 10$ star with an SNR of around 20 and a $V_{mag} = 12.5$ star with an SNR around 7. Both SNR values were assumed for the image of exposure time of 3600 seconds. RV uncertainty for a $V_{mag} = 9.5$ star was moving between 200 and 300 m/s. A spectrum of a $V_{mag} = 12.6$ star in visible had SNR 7 after 1.5 hours exposure time. The lowest brightness of observable stars was $V_{mag} = 13$. All of these parameters were valid for OES in the period before improvement in 2019.

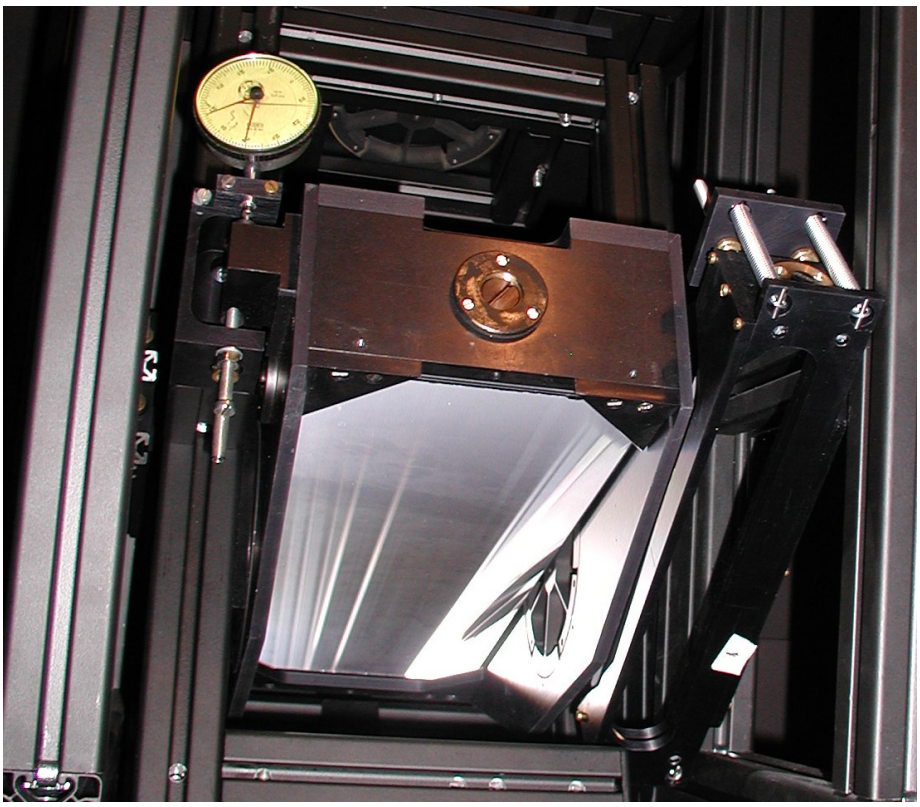

Figure 2.3: The echelle grating used in the OES - Credit: Miroslav Šlechta

2.3 Modernization in 2019

All of the previous telescope's improvements extended its options for observing. None of them changed the optical configuration of the telescope. The entire project of modernization was discussed for more than 4 years. The discussion involved experts from the field of fibre spectrographs, from ESO in Garching, from Laboratorio Nacional de Astrofisica in Brasil, and from Pontificia Universidad Católica de Chile (Šlechta, 2020).

Until the modernization of the telescope's optical system, it contained 6 optical surfaces: primary, secondary, and tertiary mirrors, two other mirrors in the optical path, and one glass plate. Scheme of the positions of the mirrors excluding glass plate and the last mirror you can see on the left side of Figure 2.4. The glass plate was used for the mechanical separation of the upper and ground floors. Without it, air would flow through the optical path and thereby affect the quality of observations (Miroslav Šlechta, 2023).

Every reflection costs a certain amount of light. This amount is increasing over time due to decreasing of the mirror's efficiency by oxidation. Not to mention impurities on the mirror surface. Theoretically, if each mirror has an efficiency of 80 %, the overall efficiency of the entire optical system is approximately 26.2 %. That is because the facility's efficiency declines exponentially depending on the number of optical surfaces. The situation is more dramatic if we consider mirrors of spectrograph (Šlechta, 2020). We know from the previous subsection about OES that the spectrograph is composed of four mirrors, one echelle grating, one prism, and one objective, overall seven optical parts. The system of telescope and spectrograph together contains 13 optical parts. Let's assume that

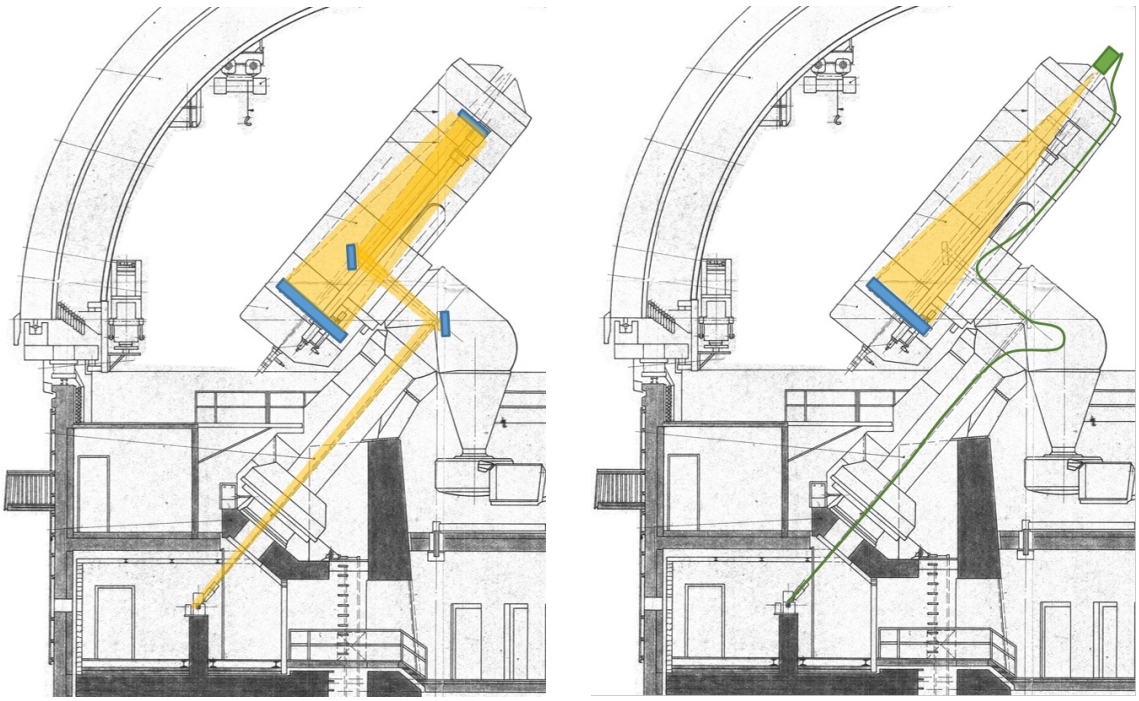

Figure 2.4: The Perek telescope before reconstruction (on the left side) and after that (on the right side) - Credit: Miroslav Šlechta (2023)

the efficiency of each part is again 80 %. In that case, the estimated efficiency of the entire system would be 5.5 % (Kabáth et al., 2020).

The modernization was done by the company TopTec Turnov, which is part of the Institute of plasma physics of the Czech Academy of Sciences, during the years 2018 and 2019. Construction work and adjustment of the optical parts took most of the time. Observations with the Perek telescope were interrupted in August 2019.

Firstly, the original secondary and tertiary mirrors and their holder constructions in the telescope's tube were removed. In Figure 2.5 you can see the primary mirror and tertiary mirror with a holder system. The secondary mirror is captured in Figure 2.6. Then there was placed new holder construction in the primary focus. This configuration was roughly balanced because the weight difference was around half of one ton. After that, the installation of the new system and laying of the cables followed. The last step was to accurately balance the telescope (Šlechta, 2020).

The primary focus is not only the beginning of the optical path. A newly located photometric camera G2-1000BI made by Moravian Instruments with resolution 1056×1027 and pixel size 13×13 µm is placed there. The final parameters of the configuration are focal length $f = 7\,\mathrm{m}$ and focal ratio $f/3.5$. This device allows one to make a photo of the current field of view. The whole construction in primary focus is captured in Figure 2.7. On the left side of the picture, you can find grey cable and after a closer look, you can find the beginning of optical fibres (Šlechta, 2020).

The new system contains 3 optical fibres. Experts recommended octagonal optical fibres Optra WT OCT by the company CeramOptec which provides uniform lightning (Miroslav Šlechta, 2023). Their length is 30 meters (Miroslav Šlechta, 2023). The active

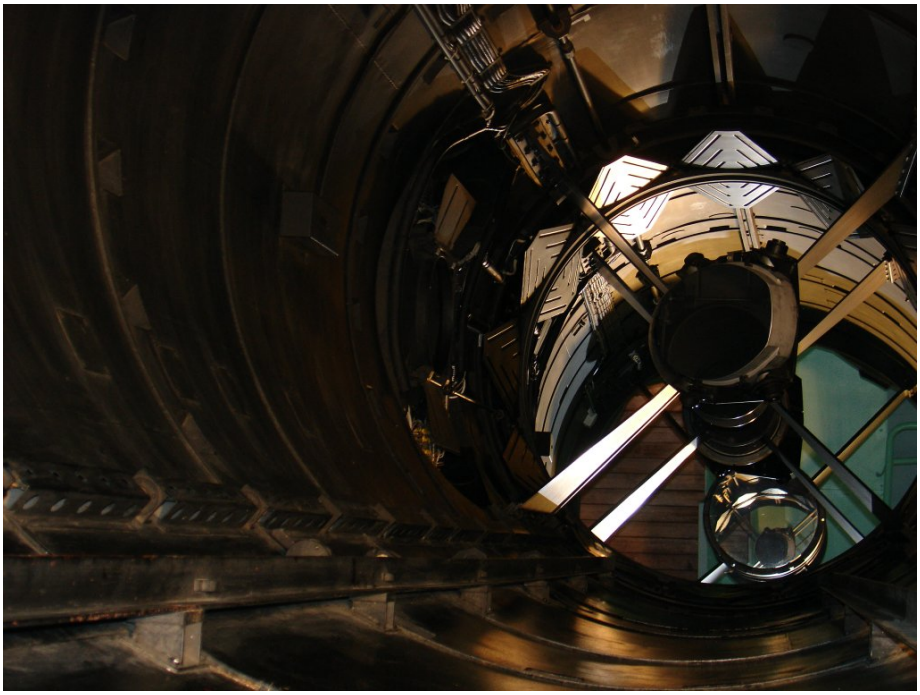

Figure 2.5: The view into the tube of the telescope, the situation before 2019 - Credit: Miroslav Šlechta (2023)

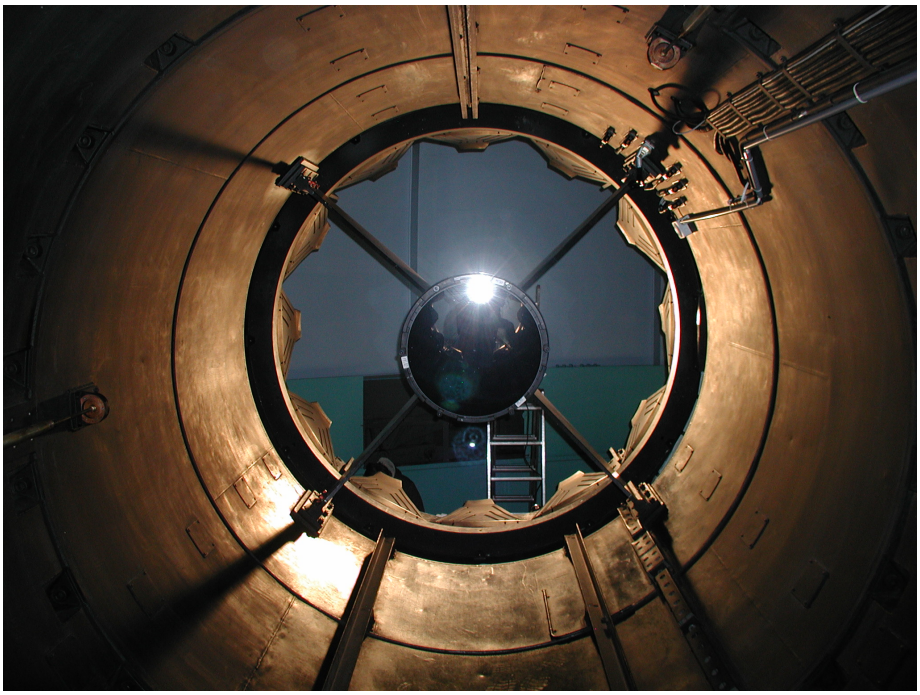

Figure 2.6: The view out of the telescope's tube before improvement in 2019 - Credit: Miroslav Šlechta (2023)

core of all fibres has a diameter of 100 µm, which matches with 2.3″ in the primary focus (typical seeing in Ondřejov). As you can see in the right side of Figure 2.4, fibres run

through the tube of declination and then through the hour axis. The final place is the Coudé room on the ground floor of the building. Fibres are diverging here. Two of them are heading to the one-line spectrograph, because of the subtraction diffused light of the sky's background. The last fibre is feeding the echelle spectrograph (Šlechta, 2020).

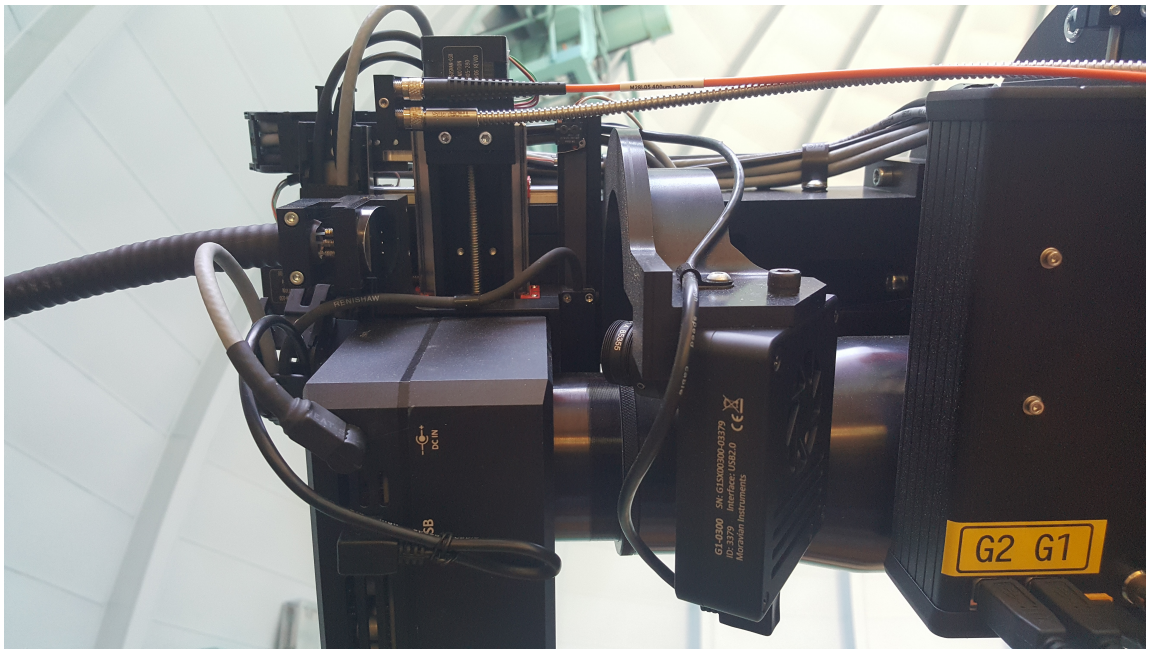

Figure 2.7: New instrument located in primary focus. On the left side of the picture can be seen three optical fibres - Credit: Miroslav Šlechta (2023)

It was necessary to place another optical element, which is adapting the focal ratio, between the end of the fibres and each slit of the spectrographs. The focal ratio in Coudé focus should be equal to 1:32 for the echelle spectrograph. However, the value of the focal ratio in the primary focus is 1:4.5 and the fibre path is changing this value to 1:4 due to the phenomenon called focus ratio degradation. The main purpose of this optical element is the reduction of the focal ratio from 1:4 to 1:32. That means 8 times enlargement of the light beam area (because of the ratio 32:4). If the diameter of the fibre is 100 µm, the new diameter will be 800 µm. The slit of the grid in OES is 600 µm wide. As a result of the light beam having a Gaussian profile, losses are insignificant. Two optical parts were placed there, the first one creates a parallel beam of light and the second one focuses it on the slit. The situation before the one-line spectrograph is more complicated. Its slit is 200 µm wide. In combination with a light beam of diameter 800 µm it leads to high loss. It was necessary to build an optical part which changes not only the focal ratio but also the shape of the light beam. This optical part is not used elsewhere in the world and is called "a free-form mirror". It contains an optical surface which follows a high-degree polynomial (Šlechta, 2020).

The new entire configuration is composed of the primary mirror, fibre cable with the special optical system and 7 optical parts of the spectrograph. Overall there are used 10 mirrors or lenses and fibre cable. According to the document by CeramOptec attached in Appendix A, the fibre cable can provide in 600 nm an efficiency of around 99.8 % per

meter of cable. The 30-meter-long fibre cable then achieves an efficiency of 91 %. If we assume again the efficiency of one optical part around 80 %, then the predicted efficiency of the entire system is about 9.8 %. The original one was 5.5 %. This means estimated efficiency increases by 80 %.

The whole work on the modernization was finished in December 2019. However, OES was commissioned in January 2020 and the one-line spectrograph was until March of the same year. Due to the pandemic situation, ceremonial commissioning took place on 26th June 2020 (Šlechta, 2020).

Chapter 3

Observation and data processing

3.1 Observed stars

Objects were selected according to several requirements. The main purpose is to compare the situation before improvement and after that. So it is necessary to select objects which were regularly observed before 2019. For example, HD 109358 which was used in Kabáth et al. (2020) is a great choice because we can compare results with the ones in this paper. Another selection factor was the altitude of an observed object. It is desirable to work with data with the least possible impact of the atmosphere. That is why images of a star around the maximum possible altitude were selected mostly. On the other hand, we selected the whole possible range of altitude of the observed star (HD 10780) in measuring the atmosphere's impact on the quality of observation.

Star name	RA	DEC	V [mag]	Spectral type
HD 10780	01 47 44.83	+63 51 09.01	5.63	K0V
HD 109358	12 33 44.54	+41 21 26.92	4.25	G0V
AD Leo	10 19 36.28	+19 52 12.01	9.52	dM3

Table 3.1: Table of the parameters of the used stars. Columns "RA" and "DEC" are equatorial ICRS coordinates J2000. Column "V" shows the apparent magnitude in the visible part of the electromagnetic spectrum. Values were obtained from SIMBAD database.

3.2 Observations

All used images were captured during observations listed in Table 3.2. "Used in" column shows in which specific measurement the data was used (ETC - Exposure Time Calculator, Comp - values comparison before modernization and after, AM - air mass influence on observations). "Observer" column informs about the operator who made the observation (DD - Daniel Dupkala, SG - Stephan Geier, PK - Petr Kabáth, MK - Marie Karjalainen, RK - Raine Karjalainen, EK - Eva Kortusová, BK - Brankica Kubátová, OM - Olga Maryeva, RN - Radek Novotný, LŘ - Luděk Řezba, MS - Marek Skarka, JSo - Jan Sloup, JSr - Jiří Srba, PŠ - Petr Škoda, MŠ - Miroslav Šlechta, MT - Miloslav Tlamicha).

Date	Star	Used in	Observer
20170506	HD 109358	Comp	PK, MT
20170511	HD 109358	Comp	MT
20180220	HD 109358	Comp	DD, JSo
20180225	HD 109358	Comp	PK, LŘ
20180403	HD 109358	RV	MS, RN
20180407	HD 109358	RV	LŘ
20180518	HD 109358	Comp	LŘ
20200111	HD 109358	RV	PK, RN, fuky
20210310	HD 109358	ETC, Comp	MS, JSl
20210324	HD 109358	Comp	MS, JSl
20210505	HD 109358	ETC	MS, JSl
20210627	HD 10780	AM	PK, EK
20210703	HD 10780	AM	MK, JSr
20210710	HD 10780	AM	OM, JSl
20210712	HD 10780	AM	RK, RN
20210715	HD 10780	AM	BK, RN
20210718	HD 10780	AM	MS, MŠ
20210811	HD 10780	AM	OM, RN
20210812	HD 10780	AM	BK, RN
20210814	HD 10780	AM	OM, EK
20210821	HD 10780	AM	MŠ, LŘ
20210906	HD 10780	AM	SG, LŘ
20210907	HD 10780	AM	SG, JSr
20210908	HD 10780	AM	SG, JSr
20210909	HD 10780	AM	MŠ, RN
20210913	HD 10780	AM	SG, LŘ
20210914	HD 10780	AM	SG, EK
20211001	HD 10780	AM	BK, JSr
20211021	HD 10780	AM	MŠ, RN
20211203	HD 10780	AM	MS, EK
20220115	HD 10780	AM	BK, LŘ
20220213	HD 10780	ETC, AM	PK, JSr
20220228	HD 109358	Comp	PK, LŘ
20220303	HD 10780	AM	BK, RN
20220313	HD 10780	AM	MS, JSr
20220412	HD 10780	AM	MK, EK
20220525	HD 109358	Comp	MS, JSl
20220618	HD 10780	AM	BK, JSr
20220830	HD 10780	AM	SG, JSr
20220902	HD 10780	AM	SG, JSr
20220905	HD 10780	AM	LŘ
20221102	HD 10780	AM	MS, JSl
20230322	HD 109358	Comp	JSo, PŠ
20230430	HD 109358	ETC	MK, EK

Table 3.2: Table of used observations

3.3 Data processing

Data were processed by the Image Reduction and Analysis Facility (IRAF), which was developed by National Optical Astronomy Observatories in Tucson (The United States, Arizona). The program is 35 years old. During that time it covered plenty of useful functions from simple ones (for instance "imexamine" - simple statistics of the image, "imarith" - image adjustments by mathematical operations, etc.) to more difficult ones (for example "apall" - extracting apertures, "ecidentify" - identification of the spectral lines, "fxcor" - calculating star radial velocity and many more). IRAF is open-source software and can be installed only on Linux systems.

Figure 3.1: Interface of IRAF

As you can see in Figure 3.1, the interface of the program is very similar to Linux Terminal. Commands and function parameters are simply written to the command line and executed. Users can make scripts of many functions through text file .cl, which can be executed by IRAF. The part of results can be listed below the command line and plots or other results can be viewed by "irafterm" (Figure 3.2).

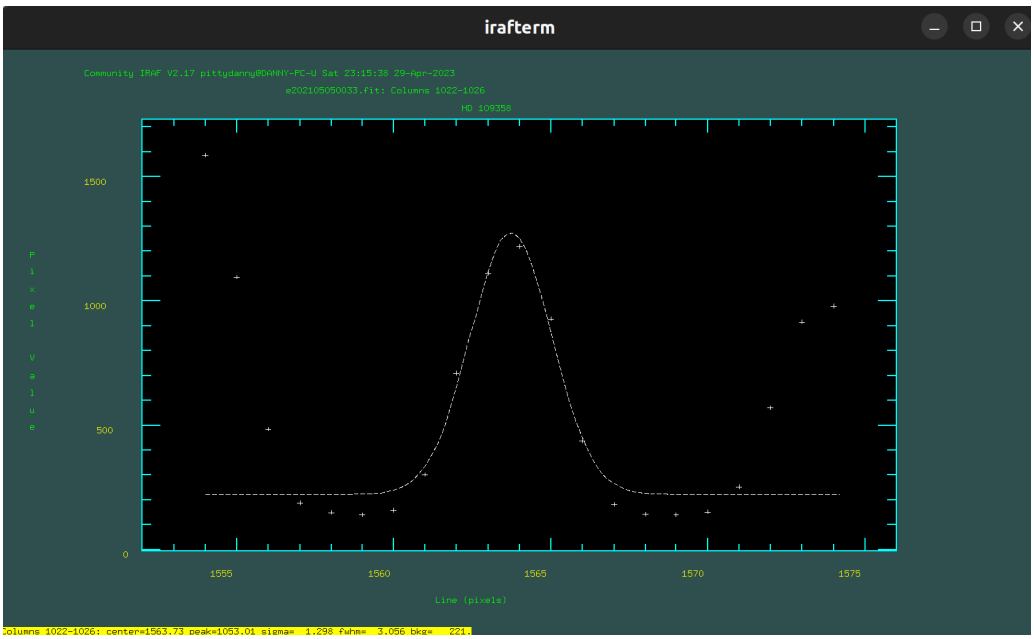

Figure 3.2: Window of the irafterm

IRAF is compatible with the image display tool SAOImageDS9. Images created by OES are in FITS (Flexible Image Transport System) format. In Figure 3.3 you can notice that spectra images contain many horizontal lines - apertures, which are slightly bent. The whole one-dimensional spectrum would never fit in the image. That is the reason, why is the spectrum divided into parts placed on top of each other. There are about 56 apertures. The ones on the edges of the image are slowly passed into invisible parts of the light spectrum.

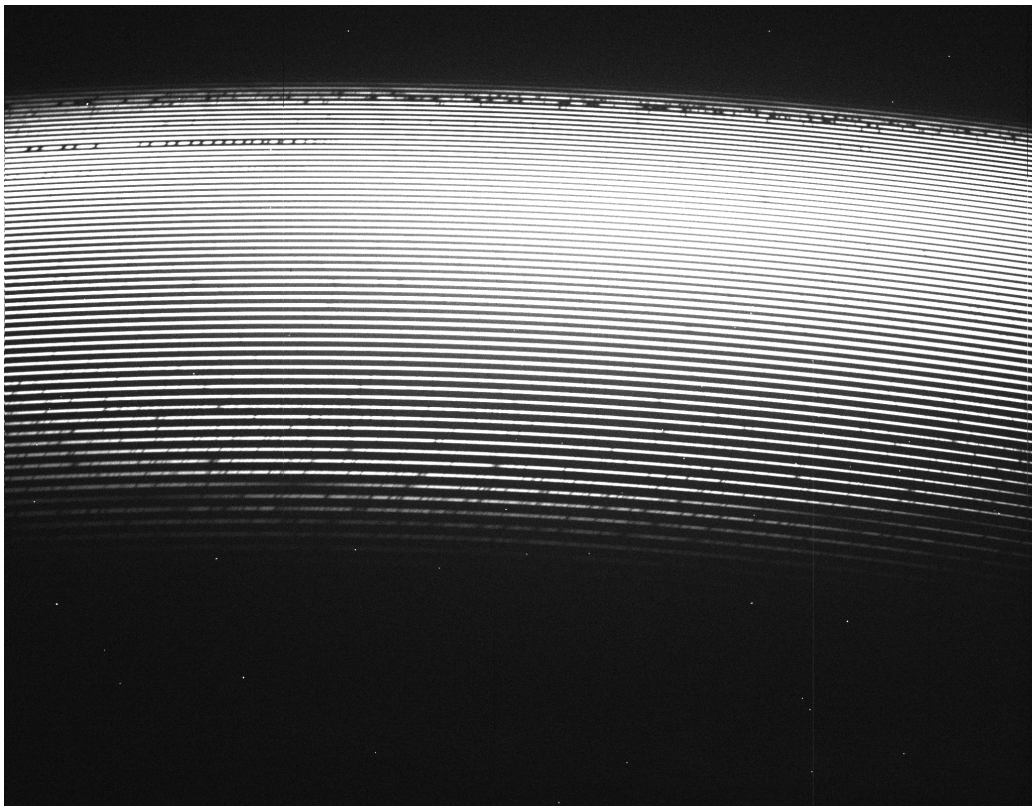

Figure 3.3: Image (e202105050033.fit) of spectrum of HD 109358 made in 5th May 2021

3.3.1 RV measurement

For measurement of star radial velocity, we need to process data from raw echelle spectrum to one-dimensional spectrum where we can much more easily measure radial velocity. However, images of the observed star contain many flaws caused for example by cosmic rays, vignetting or the chip itself. Therefore, more types of images are made during observation. These images are stored in separate folders - object, zero, flat and comp. The object folder contains images of the observed object and a bright star (Figure 3.4a). Bias frames (Figure 3.4b) with zero exposure time which exclude readout noise from object images are saved into the zero folder. Flat frames (Figure 3.4c) usually capture a homogeneously lit area and are used for removing the negative influence of the used optical system as vignetting. In the last folder, we can find images of the comparative thorium-argon (Th-Ar) spectrum (Figure 3.4d).

(a) Object image of Vega

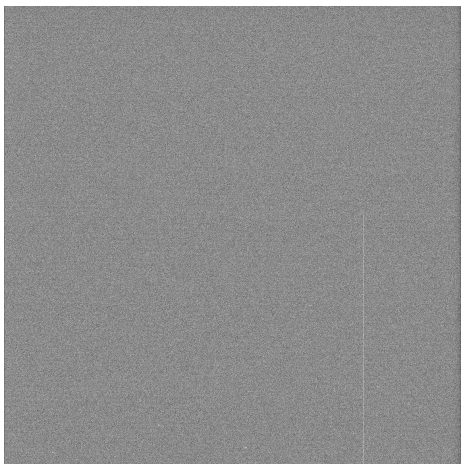

(b) Bias image

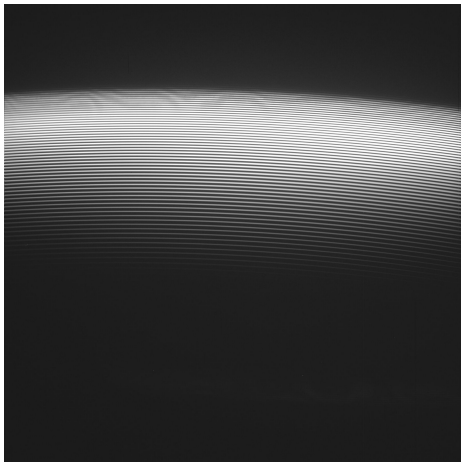

(c) Flat image

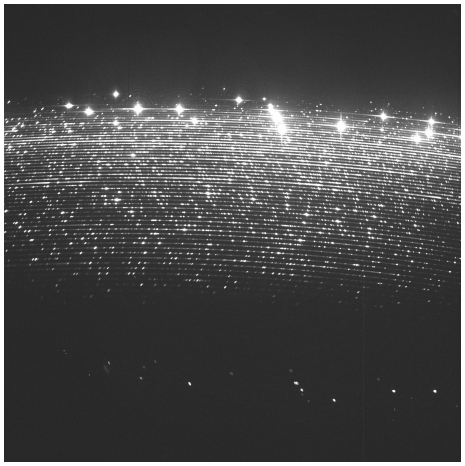

(d) Comparative Th-Ar image

Figure 3.4: All needed images for RV measurement - Credit: website about OES

First of all, it is necessary to remove hits of cosmic rays and bad pixels of the chip by processes "cosmicrays" and "fixpix". After that is image cropped to contain only the visible part of the spectrum.

The second step is creating master-frames of bias and flat images. Firstly is made masterbias by command "zerocombine". This master-frame is then subtracted by the "imarith" command from all of the flat frames, which are combined into masterflat by "flatcombine" later.

As mentioned in the previous chapters, the echelle spectrum consists of 56 apertures - parts of the original one-dimensional spectrum. These apertures are slightly bent and their shape is needed to define in the following step. It is recommended to use the image of the bright star, but it is possible to use object image as well. From this image is made aperture template image by task "apall". After that is created normalized flat by task "apflatten". This image repairs irregular illumination of the image caused by spectrograph and telescope.

In the next step, we will use masterbias and normalized flat for object and comparison images correction. These images are subtracted by masterbias and then divided by nor-

malized flat. All of these tasks are made by "imarith". After that follows the extraction of spectra. For that is used command "apall" and the result of that is a two-dimensional spectrum.

Now we will use Th-Ar images for calibrating units on the horizontal axis. Originally, the two-dimensional spectrum uses as unit pixels, but for our goal, it is necessary to change pixels to wavelength (usually Ångström). Light from the observed star is affected by the atmosphere of Earth. Spectrum then includes absorption lines of thorium and argon which are always on the same wavelength. These reference lines are used for the identification of other lines by task "ecidentify". This task is always made manually by comparing absorption lines with spectrum lines atlas. Changing pixels to wavelength in all object images is made by task "dispcor".

One of the last things is spectrum normalization by task "continuum". Unfortunately, the result of this task is very subjective. The final one-dimensional spectrum is made by several steps: in "sarith" task are firstly divided non-normalized images by normalized ones. The result is images with a pure continuum. Secondly, we merge non-normalized images into a one-dimensional spectrum. The same thing is made with pure continuum images. The third and last step is dividing the non-normalized one-dimensional spectrum by the pure continuum one-dimensional spectrum. This gives us the final one-dimensional spectrum of the observed object.

In the end, we can measure radial velocity from the one-dimensional spectrum by task "fxcor". An important thing is a heliocentric correction by task "rvcorrect" which will include the movement of the Earth around the Sun and the Earth's rotation. For this task, it is needed to fill the parameters of observation in the file "obsdb". The last step is using the command "fxcor" again. The RV values will be listed in the text file including the error of measurement. The whole data process is described in more detail in the bachelor thesis by Štegner (2020).

For my work, I have used scripts made by the Ondřejov Exogroup members. These scripts make the data process much easier and faster. You can find them in Appendix C.

3.3.2 SNR measurement

SNR is always measured on the one concrete point of the image. It is necessary to measure the same point of the spectrum. Apertures of the same star are moving over time relative to the edges of the image. This motion is caused by different external conditions during observation. During measuring the SNR of more images it is crucial to check the position relative to the spectrum. The best way to follow it is to find some specific aperture and relate the position in the spectrum to this aperture. I have chosen the region of telluric lines as a base and numbered this aperture with zero, as you can see in Figure 3.5.

I decided to measure SNR in three areas so that I could better observe the effect of wavelength on the results. All of them are located in the middle of the horizontal axis of the image. The vertical positions of these areas were chosen firstly by the biggest number of counts. Now, it is labelled as the 2nd area. The first and third areas are 10 apertures up and down from the middle one.

Wavelengths of these locations are listed in Table 3.3 and were estimated from the order of the apertures and their parameters listed in Koubský et al. (2004). As I mentioned

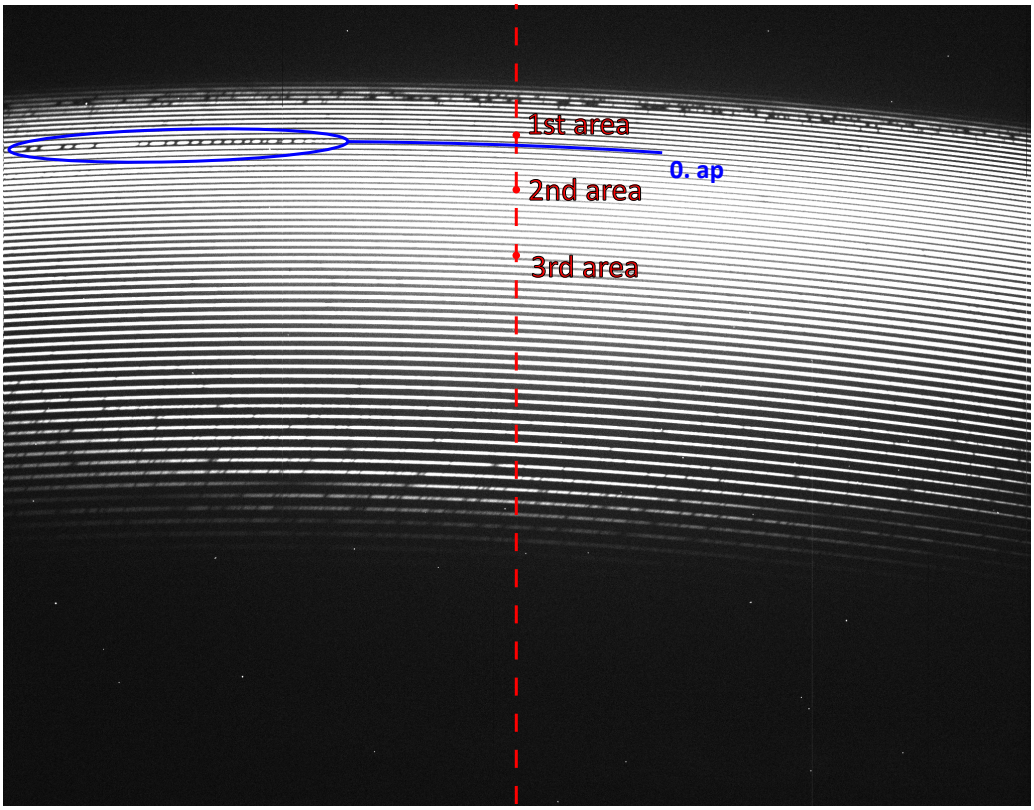

Figure 3.5: Region of telluric lines and its aperture is marked by blue colour. The red dashed line marks the centre of the image. The red points denote locations of measuring.

above, apertures are slowly moving over time. I have noticed the positions of all three areas and base aperture throughout the time of observing. You can find them in Table 3.4.

The procedure of measurement is the following. It is necessary to open IRAF in the file where are located images to measure. Moreover, it is needed to open SAOImageDS9. That is possible through the command "!ds9&" in IRAF. In SAOImageDS9 we will open a required image and then execute the command "imexam" in IRAF. This will start special mode which is noticeable by the flashing cursor. After clicking on the SAOImageDS9 window we have to find the needed position where we want to measure SNR. The cursor can be controlled not only by the mouse but also for finer movement by arrow keys on the keyboard. Once the cursor is at the desired location we can press "k" and this will open the irafterm window with the plot of the peak's profile and in the lower part of the window is located a yellow line with parameters of the peak. Usually, it is needed to enlarge the window, because all parameter values do not fit into the opened window. We will note down parameters "peak", "fwhm" and "bkg" which correspond with peak counts, full width at half maximum and bias. A combination of clicking somewhere in the image and pressing "q" will save the cursor's position. Pressing "q" will also stop this mode. Unfortunately, it is not possible to make measurements of all three points at one time. After measuring one point it is necessary to quit imexamine mode a then again start this mode. The cursor should move to the saved position and it is possible to continue with measuring other points. For moving between apertures I used arrow keys because it

Location	Wavelength
1st area	709 nm
0th aperture	682 nm
2nd area	591 nm
3rd area	506 nm

Table 3.3: Wavelengths of the selected areas

	2017	2018	2021	2022	2023
1st area	$1024, 1497$	$1024, 1499$	$1024, 1564$	$1024, 1567$	$1024, 1551$
0th aperture	$1024, 1476$	$1024, 1479$	$1024, 1543$	$1024, 1546$	$1024, 1531$
2nd area	$1024, 1387$	$1024, 1390$	$1024, 1455$	$1024, 1457$	$1024, 1442$
3rd area	$1024, 1256$	$1024, 1258$	$1024, 1323$	$1024, 1326$	$1024, 1311$

Table 3.4: Coordinates of the areas in the image during the years

is needed to count apertures during moving in the smaller zooming window. Position I always checked with the values in Table 3.4.

Chapter 4

Results

4.1 RV results

For radial velocity measurements, were selected images of HD 109358 with exposure time 600 seconds and with a maximal possible altitude of the star. It is about 81° above the horizon. Results are plotted in the plot 4.1. Observations were selected from the period before modernization (grey crosses) and after modernization (black crosses). The red-hatched rectangle shows the modernization period when the telescope was out of service.

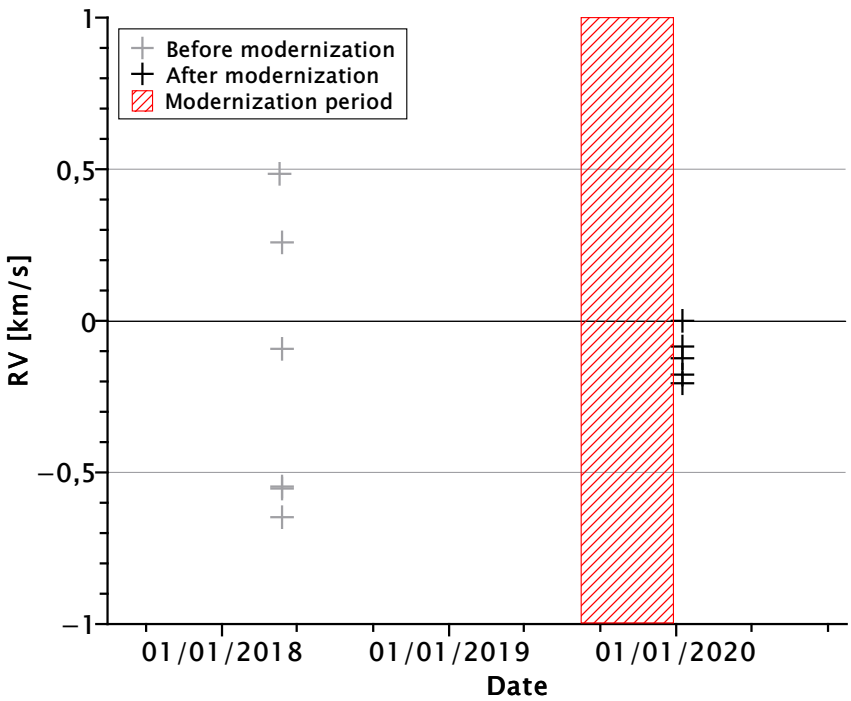

Figure 4.1: Comparison of RVs before and after modernization - Before modernization values are marked by grey crosses and after modernization values are marked by black crosses. The red rectangle represents the modernization period

As you can see in the plot 4.1, the range of values measured before modernization is much bigger than the one measured after modernization. Values measured before modernization are in the range from -0.65 to $0.5\ \mathrm{km/s}$. However, measured values in the period after modernization are in the range from -0.09 to $-0.20\ \mathrm{km/s}$. The dispersion of the values can be described by standard deviation. The standard deviation of the measured RV values is for the data before modernization $0.43\ \mathrm{km/s}$ and for the data after modernization $0.07\ \mathrm{km/s}$.

Data were captured at the similar altitude above the horizon so air mass should not have any influence on the difference in the quality of observations. Unfortunately, there is no available information about seeing during these observations. If we assume other conditions were similar and observations were not dramatically affected by weather, we can claim that the quality of observation was positively changed by the modernization of the optical path.

4.2 SNR results

In the next part of this chapter, we will compare and discuss measured SNR values. The first section is about observing SNR over a long-term period. Right here we can compare measured SNR values from the period before and after modernization in 2019. The second part describes how much is the quality of observation affected by air mass. The next part includes the exposure time calculator and its comparison with the one from Kabáth et al. (2020). In the last part, we will try to calculate RV uncertainty from SNR values.

4.2.1 Long-term data sets and SNR

Firstly, before and after modernization SNR values were compared. In this section were used 6 observations before and 5 observations after modernization. The main two criteria were exposure time and altitude. All images were captured for 600 seconds and the altitude of HD 109358 was the maximal possible, around 81°.

SNR was measured in three different areas of each image. These results are sorted by the wavelength of the measured area so in Graphs 4.2a, 4.2b and 4.2c you can find results from 709 nm, 591 nm and 506 nm. The comparison of all results is plotted in Graph 4.2d. The red-hatched rectangle in the following graphs represents the period when the telescope was out of service due to modernization.

As we can see in the graphs above, the area of 591 nm reaches the highest values. It is followed by the area of 506 nm and the lowest values were measured in the area of 709 nm. This is not a surprising finding if we assume the quantum efficiency of the used CCD chip. According to the curve of the quantum efficiency in website of IAA-CSIC (2023) attached in Appendix B, we can estimate quantum efficiency values for the selected wavelengths: for 709 nm it is 88 %, for 591 nm 96 % and the last 506 nm has 94 %. Now we can see that measured SNR values correspond with the quantum efficiency of the CCD chip.

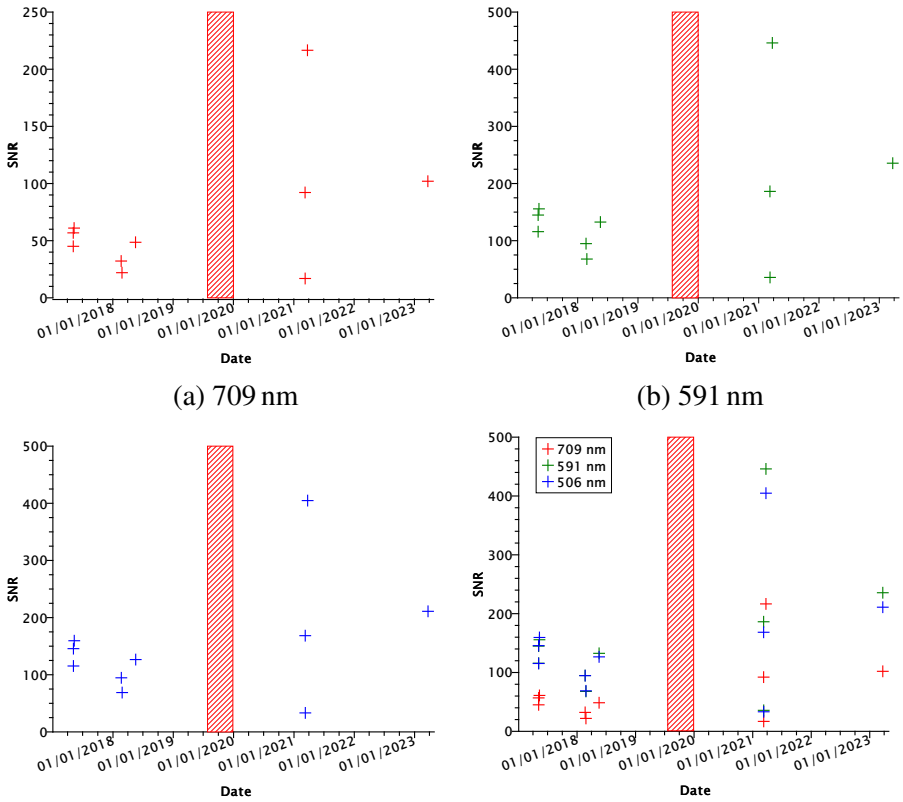

(a) 709 nm

(b) 591 nm

(c) 506 nm

(d) Direct wavelength comparison

Figure 4.2: Comparison of SNR values measured before and after modernization in 709 nm, 591 nm, 506 nm and their direct comparison - Values are marked by crosses (709 nm - red crosses, 591 nm - green crosses, 506 nm - blue crosses). The red rectangle represents the modernization period.

Wavelength [nm]	Medians before modernization	Medians after modernization	Increasing by [%]
709	46.8	97.1	107
591	124.2	210.9	70
506	121.0	189.7	57

Table 4.1: Comparison of medians of SNR values from the periods before and after modernization

Moreover, we can see an evident increase in SNR values after modernization in 2019. This trend can be described by changes in the median of the measured data. In this case, the average is not applicable due to distortion by possibly measured extreme values. On the other hand, the median is not affected by extremes so in this case is much more suitable. Medians for all measured wavelengths of both data sets are listed in Table 4.1. Furthermore, there is mentioned by what percentage the values have changed.

We have tried to estimate theoretical efficiency increase in the section Modernization in 2019 of the second chapter. The estimated efficiency was 80 %. The real values in Table 4.1 are really very close to our estimation. The biggest improvement is observed in the redder part of the spectrum. This is probably caused by better transmission efficiency of the fibre cable in 509 nm (Appendix A) than the original optical path provided.

4.2.2 Influence of the air mass on the SNR

In the next section, we examined the influence of air mass on the quality of observations. Images of the star HD 10780 were used for this task. A total of 31 images captured in the after-modernization period were used and the altitude of the star varies between 32° and 76°.

It is needed to know the altitude of the observed star for calculating equivalent air mass. Altitude h should be converted to true zenith angle z_t by Equation 4.1. The true zenith angle is defined as the angular distance between the true position of the observed star and the zenith. However in this case we work with altitudes higher than 30° above the horizon so observations are not so much affected by refraction. According to Bennet (1982), refraction in 30° above the horizon causes the object to move by several units of arcminutes. Therefore we will neglect refraction further. According to Young & Irvine (1967), air mass can be calculated from true zenith angle z_t by Equation 4.2.

$$z_t = 90° - h \tag{4.1}$$

$$X = \sec z_t [1 - 0.0012(\sec^2 z_t - 1)] \tag{4.2}$$

This model provides valid values up to 80° of the zenith angle. As we work with altitude up to 30° which corresponds with zenith angle 60°, we can use this equation in our work. Graphs 4.3a, 4.3b and 4.3c show the dependence of SNR on the acting air mass in three different wavelengths. All values are directly compared in Graph 4.3d.

As we can see in the graphs, there is no evident relation between SNR and air mass affecting each observation. It is important to remind that star was observed in the range of air mass between 1–2. These values correspond with altitude in range 30–90 °. According to these results, observations of objects higher than 30° above the horizon should not be affected by air mass. It seems that the quality of observation is more affected by other conditions, especially by current weather, humidity or cloudiness.

4.2.3 Exposure time calculator and the SNR

One of the main goals of this thesis was to make an exposure time calculator. Stars HD 109358 and AD Leo were selected for this task because the same stars were included in the ETC from Kabáth et al. (2020). We will be able to compare both ETCs with each other. Images of HD 109358 were taken with exposure times of 60, 180, 480, 600 and 1800 seconds and an image of AD Leo with exposure time of 600 seconds. As in previous cases, all used images were made at the maximum possible altitude of each star, for HD 109358 it is around 81° and for AD Leo it is around 60°. In Graphs 4.4a, 4.4b and 4.4c are

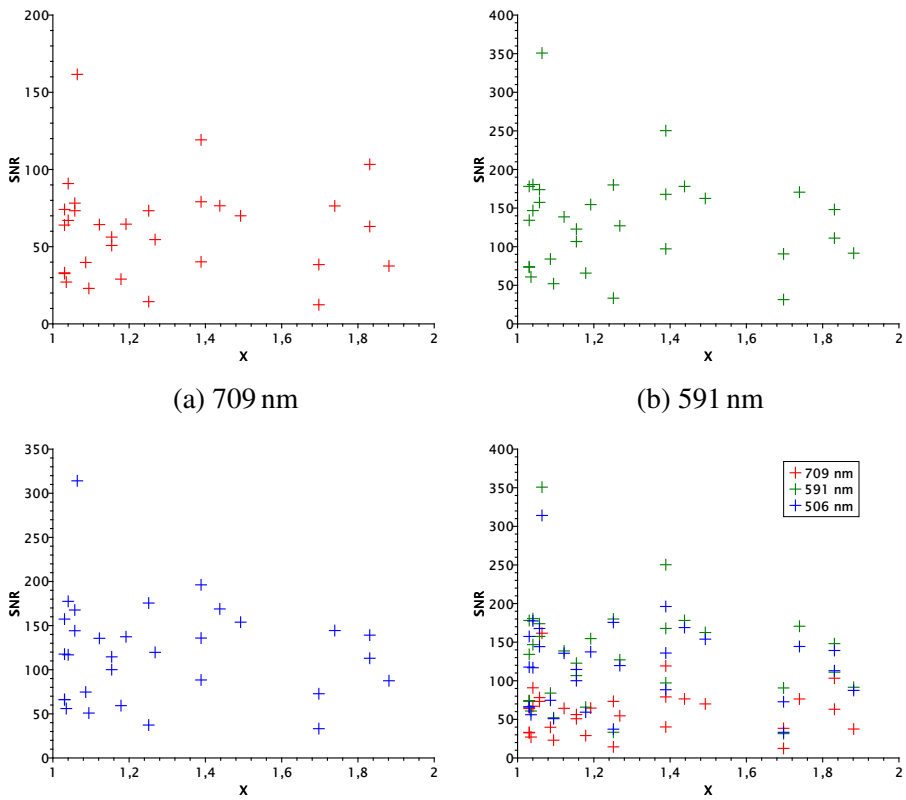

(a) 709 nm (b) 591 nm

(c) 506 nm (d) Direct wavelength comparison

Figure 4.3: Air mass influence on SNR values measured in 709 nm, 591 nm, 506 nm and their direct comparison - Values are marked by crosses (709 nm - red crosses, 591 nm - green crosses, 506 nm - blue crosses).

ETCs for all selected wavelengths and comparison of these values you can find in Graph 4.4d.

In Graph 4.4d, we can notice that the best SNR values are again measured in 591 nm. Very similar quality is in 506 nm and the worse values were measured in 709 nm. This result confirms the previous ones in the last two sections. A different situation can see with the star AD Leo. Here is the red part in relation to other parts of the spectrum much better than the one of HD 109358. It is even better than the blue part of the same spectrum. This can be caused by another spectral type of observed star. HD 109358 is a solar-type star (G type), but AD Leo is M type star. That means this star is colder and its maximum of emitted electromagnetic radiation is shifted to the redder part of its spectrum.

Furthermore, we will only work with measured SNR values in 591 nm. Graph 4.5a is the calculated exposure time calculator for OES after modernization. We can see there measured values of HD 109358 and AD Leo (blue and red crosses) and theoretical lines of dependence of SNR on the exposure time of the image.

Next Graph 4.5b compares newly created ETC in Graph 4.5a with ETC from the paper Kabáth et al. (2020). New results are displayed by blue and red crosses (HD 109358 and AD Leo). New theoretical dependencies are shown by solid lines. Black crosses and dashed lines represent original results from Kabáth et al. (2020).

If we directly compare SNR values of the HD 109358 of the equivalent exposure times from ETC by Kabáth et al. (2020) and new values, we will get increasing in SNR value by an amount between 55 and 136 %. In the chapter Modernization in 2019 estimate of the spectrograph's efficiency was mentioned. It was 9.9 % and the increase caused by modernization was predicted around 80 %. We can see that the measured increase in SNR is obviously caused by modernization itself.

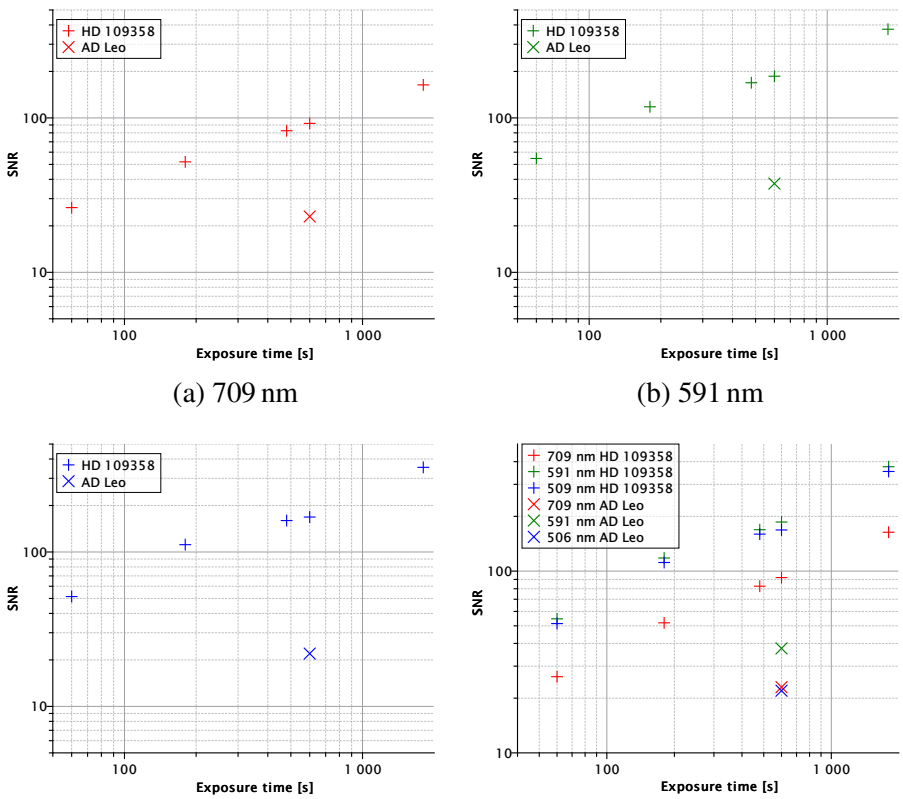

(a) 709 nm

(b) 591 nm

(c) 506 nm

(d) Direct wavelength comparison

Figure 4.4: ETCs for 709 nm, 591 nm, 506 nm and their direct comparison - Values are marked by crosses (709 nm - red crosses, 591 nm - green crosses, 506 nm - blue crosses).

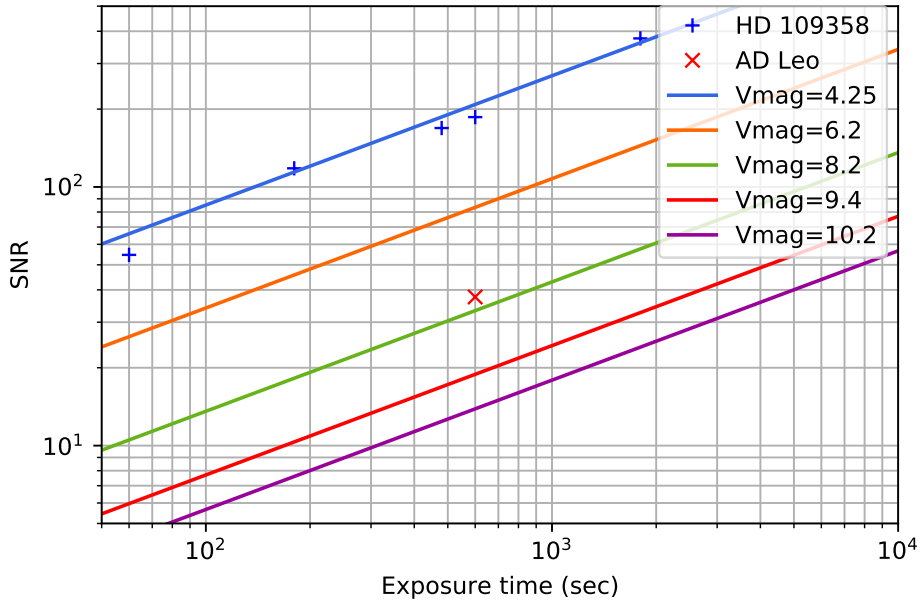

(a) ETC for OES after modernization in 2019

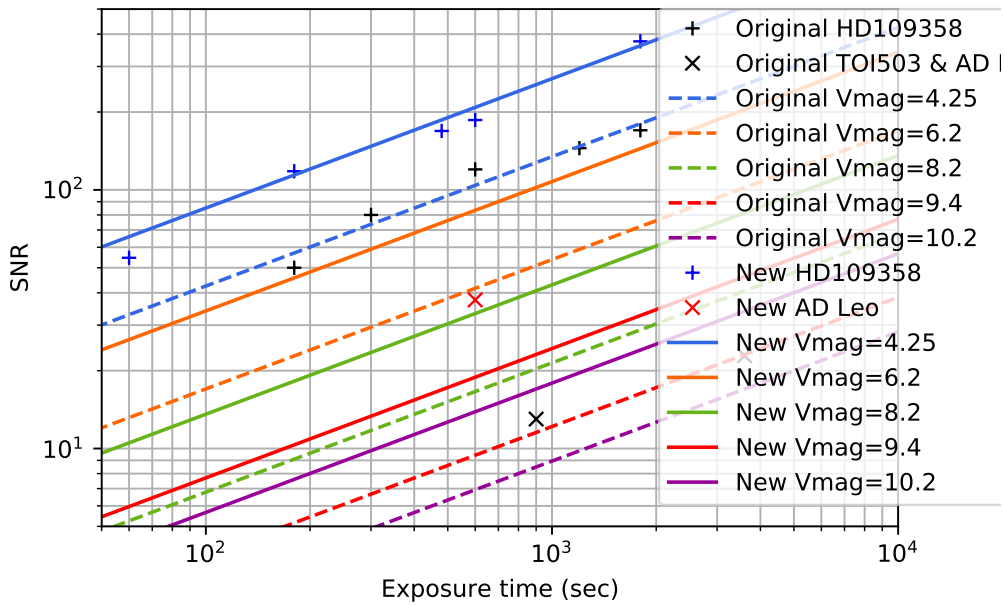

(b) Comparison of new ETC with the original one from Kabáth et al. (2020) - Concrete SNR values are marked by crosses (original values - black crosses, HD 109358 and AD Leo after modernization - blue and red crosses). Theoretical lines for the period before modernization are marked by dashed lines and for the period after modernization by solid lines.

Figure 4.5: New ETC and its comparison with the original one from Kabáth et al. (2020)

4.2.4 Theoretical values of RV uncertainties

To the end, we can calculate theoretical values of RV uncertainties by Equation 1.12 from Gustafsson (1992). According to Kabáth et al. (2020), needed spectrograph parameters are following:

$$\Delta\lambda = 5900\,\text{Å}$$
$$R = 50\,000$$
$$C = 6.5 \times 10^{12}$$

$$\sigma_{RV} = C \times (SNR)^{-1} \times \Delta\lambda^{-0.5} \times R^{-1.5}$$

Original RV uncertainty for a $V_{mag} = 9.5$ star mentioned in Kabáth et al. (2020) was about 200–300 m/s. Unfortunately, there were not mentioned which exposure times were needed for these values and from which part of the spectrum were SNR needed for this theoretical range measured. For further work, we will use SNR values of HD 109358 from the original ETC. These values are listed in Table 4.2 in the "Before" column and equivalent RV uncertainties are mentioned in the next column. In the "After" column, you can find SNR values of HD 109358 measured in 591 nm after modernization in 2019.

Exposure time [s]	Before		After	
	SNR	σ_{RV} [m/s]	SNR	σ_{RV} [m/s]
60	-	-	54.6	138.6
180	50	151.4	118.1	64.1
300	80	94.6	-	-
480	-	-	169.0	44.8
600	120	63.1	186.2	40.6
1200	145	52.2	-	-
1800	170	44.5	375.2	20.2

Table 4.2: Theoretical values of RV uncertainties for a $V_{mag} = 4.25$ star calculated from SNR values - The "Before" column includes SNR values from Kabáth et al. (2020) and equivalent calculated RV uncertainties. The "After" column includes SNR values measured after modernization in 2019 and equivalent RV uncertainties.

If we assume similar conditions during observation, we can see an evident decrease in RV uncertainties caused by the modernization of the optical path. It is important to remind that Equation 1.12 is valid only for the G-type stars.

Conclusions

The main goal of this thesis was to find out what effect had the modernization of the Perek telescope in 2019 on the quality of observation. Until 2019, the optical path from the tube of the telescope to spectrographs consisted of 5 mirrors and one glass plate. Modernization in 2019 replaced 4 mirrors with optical fibres. In the thesis were used observations made between 2017 to 2023.

Data sets were processed by the software IRAF and were measured by two methods: radial velocities and signal-to-noise ratio. The first method compared measured radial velocities of HD 109358 before and after modernization. From Graph 4.1 it is obvious that the range of measured radial velocity during one observation has decreased. The standard deviation of the values changed from $0.43\,\mathrm{km/s}$ to $0.07\,\mathrm{km/s}$. Unfortunately, it is not clear what conditions affected the observations. If we assume the same conditions during both observations, we have the first proof of successful modernization.

Secondly, we watched values of signal-to-noise which were measured in three areas of each image in 506 nm, 591 nm and 709 nm. We found out that the best values were always measured in 591 nm. Very similar values but still a little worse were measured in 506 nm and the worst ones were measured usually in 709 nm. These results are related to the quantum efficiency curve of the used CCD chip which is attached in Appendix B. In Graph 4.4d we could see better results of values from 709 nm than from 506 nm in the case of AD Leo. This is probably caused by the observed star itself. AD Leo is M type star but HD 109358 is G type star. As AD Leo is cooler, its maximum of emitted light is in the redder part of its spectrum.

SNR values were first compared in the long-term period. More specifically, SNR values measured in the periods before and after modernization in 2019 were compared. In Graph 4.2d we can see the change in the range of the measured SNR values. This change was described by the medians of both data sets. In Table 4.1, we can see those medians increased by 57–107 %.

After that, we showed on measured SNR values of HD 10780 in Graph 4.3d that the quality of observation is not strictly dependent on air mass if the observed object is located higher than 30° above the horizon. Quality of observation is much more dependent on current observing site conditions.

In the third part, the exposure time calculator was made (Graph 4.5a) and it was compared with the one from Kabáth et al. (2020) (Graph 4.5b). According to the comparison of equivalent SNR values, we found out that SNR values measured after modernization are higher by 55–136 %.

To conclude, it is certain that the efficiency of the telescope increased with the modernization of the optical path in 2019. The estimated efficiency increase of the entire

spectrograph was predicted in the section Modernization in 2019 and was around 80 %. This efficiency increase undoubtedly led to the decrease of the standard deviation of RV measurement, to the increase of all SNR values and to the decrease of the theoretical RV uncertainties in Table 4.2.

A possible continuation of this work could be making one observation night of one star with different exposure times to eliminate the influence of weather and other conditions. Furthermore, it would be worth measuring the influence of fibre cable on different wavelengths, for example in 10 different wavelengths. Additional measurements of standard stars and other objects can reveal even more refinement of our result. We could try to measure the influence of the seeing etc... However, the telescope upgrade was successful and we demonstrated that the increase in the telescope's efficiency to collect light is much higher than before the fibre upgrade.

Appendix

A Parameters of the fibre cable

CeramOptec®

Optran® UV, Optran® WF
Silica / silica fiber with optional buffers

Superior performance and fiber optic properties from UV to IR wavelengths: CeramOptec®'s Optran® UV / WF fibers are available in a range of core diameters and assemblies, tailored to your specific application needs.

Wavelength

Optran® UV	190–1200 nm
Optran® WF	300–2400 nm

Numerical aperture (NA)

Low	0,12 ± 0,02
Standard	0,22 ± 0,02
High	0,28 ± 0,02

Advantages

- Pure synthetic, fused silica glass core
- High resistance against laser damage
- Step-index profile
- Special jackets available for high temperatures, high vacuum and harsh chemicals
- Very low NA expansion
- Biocompatible material
- Sterilisable using ETO and other methods

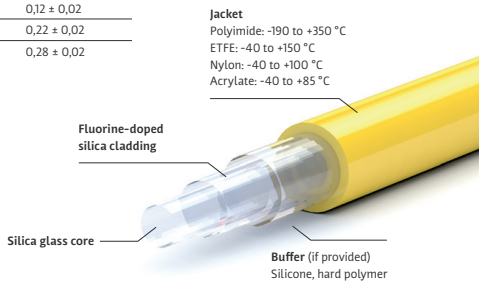

Technical data

Wavelength / spectral range	Optran® UV: 190 – 1200 nm Optran® WF: 300 – 2400 nm
Numerical aperture (NA)	0,12 ± 0,02 | 0,22 ± 0,02 | 0,28 ± 0,02 or customised
Operating temperature	-190 to +350 °C
Core diameter	Available from 25 to 2000 µm
Standard core / cladding ratios	**1:1,04 | 1:1,06 | 1:1,1 | 1:1,15 | 1:1,2 | 1:1,25 | 1:1,4** or customised
OH content	Optran® UV: high (> 700 ppm) Optran® WF: low (< 1 ppm) Fibers with OH contents < 0,25 and < 0,1 ppm are available upon request
Standard prooftest	100 kpsi (nylon, ETFE, acrylate jacket) | 70 kpsi (polyimide jacket)
Minimum bending radius	50 × cladding diameter (short-term mechanical stress) 300 × core diameter (during use with high laser power)
Product code	See reverse side

Headquarter

CeramOptec® GmbH, Siemensstr. 44, 53121 Bonn, Germany
Sales / Development, Brühler Straße 30, 53119 Bonn, Germany
Phone: +49.228.979 670, Fax: +49.228.979 6799
sales@ceramoptec.de, www.ceramoptec.com

Production sites

CeramOptec® GmbH Brühler Straße 30, 53119 Bonn, Germany
CeramOptec® SIA Domes iela 1a, 5316 Livani, Latvia

Attenuation values

The following diagrams provide an overview of attenuation values relative to the wavelengths:

Optran® UV

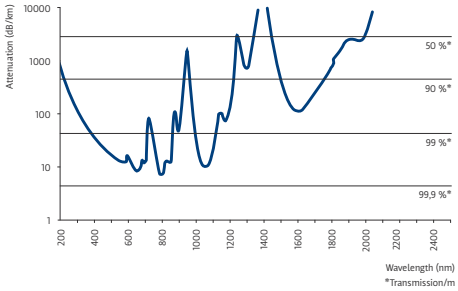

Optran® WF

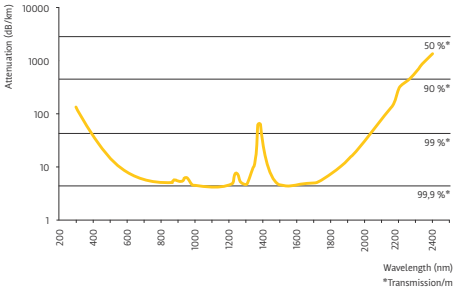

Applications

First choice for applications including spectroscopy, medical diagnostics, medical technology, laser delivery systems and many more.

Product code key using the example of WF 300/330 (H)(B)N (28)

1	**Fiber type**	UV = Optran® UV | WF = Optran® WF | WFGE = Optran® WFGE | HUV = Optran® HUV HWF = Optran® HWF
2	**Standard core / cladding ratios**	Core ø (µm) / Cladding ø (µm)
3	**Buffer**	H = hard polymer buffer | No information = silicone buffer
4	**Colour**	B = black | BL = blue | W = white | Y = yellow | R = red | G = green No information = transparent
5	**Jacket material**	A = acrylate jacket (no buffer) | N = nylon jacket (silicone or hard polymer jacket) T= ETFE jacket (silicone or hard polymer buffer) | P = polyimide jacket (no buffer)
6	**Numerical aperture (NA)**	12 = 0,12 | 28 = 0,28 | No information = 0,22 (standard)

Your advantages

- Over 500 Optran® UV and Optran® WF fibers in stock
- Non-standard diameters and NA values available
- Option of fully customised fiber production
- A complete solution for all your performance needs
- GMP and ISO 9001 compliant manufacturing environment
- CE mark

Headquarter

CeramOptec® GmbH, Siemensstr. 44, 53121 Bonn, Germany
Sales / Development, Brühler Straße 30, 53119 Bonn, Germany
Phone: +49.228.979 670, Fax: +49.228.979 6799
sales@ceramoptec.de, www.ceramoptec.com

Production sites

CeramOptec® GmbH Brühler Straße 30, 53119 Bonn, Germany
CeramOptec® SIA Domes iela 1a, 5316 Livani, Latvia

B Parameters of the CCD camera

...SEE the Future

Princeton Instruments

VersArray: 2048B

The Princeton Instruments VersArray: 2048B is a high-performance, full-frame digital camera system that utilizes o back-illuminated, scientific-grade CCD. With a 2048 x 2048 imaging array, 100% fill factor, and 13.5 x 13.5 µm pixels, this system provides a very large imaging area with very high spatial resolution. Dark current is reduced to near zero with liquid-nitrogen cooling*, even for long exposures. The large field of view, exceptionally high quantum efficiency, low readout noise, and low binning noise make this camera ideal for a variety of low-light applications, including macro-imaging of chemiluminescence.

Applications: Astronomy, Large format imaging, Phosphor/scintillator imaging, Chemiluminescense

*For convenient thermo-electric cooling, the CCD is also available in the latest PIXIS platform. See PIXIS: 2048 datasheet for further information.

Features	Benefits
2048 x 2048 imaging array 13.5 x 13.5 µm pixels	High-resolution, megapixel sensor
Back-illumination	Highest QE (>90%) possible
Low-noise readout	Able to measure smaller signals
Flexible binning and readout	Increases light sensitivity while increasing the frame rate
100 kHz/1MHz readout speed	Selectable readout to optimize for low noise or high speed operation
16-bit digitization	Quantifies both bright and dim signals in the same image
Kinetics (optional)	Allows faster frame rates when only partial number of rows are shifted
Liquid-nitrogen cooling	Very long integration times for higher sensitivity
F-mount	Easily attaches to standard lenses or optical equipment
USB2.0	Plug-n-play interface for easy setup
PCI interface	Works with PC
Fiber optic interface (optional)	For remote operation. Available for USB2.0 and PCI
Video output	Compatible with standard video equipment

...SEE the Future

VersArray: 2048B Specifications

CCD image sensor		e2v CCD42-40; scientific grade, back-illuminated, full frame CCD	
CCD format		2048 x 2048 imaging pixels 13.5 x 13.5 µm pixels; 27.6 x 27.6 mm imaging area (optically centered)	
Grade*		≤ 3 column for Grade 1 (Contact factory for detailed grade specifications)	
		Typical	Maximum
Linear full well	single pixel 2 x 2 binned pixel	>80,000 e- >800,000 e-	
Read noise	1-MHz digitization 100-kHz digitization	8 e- rms 3.5 e- rms	10 e- rms 5 e- rms
Cooling Temperature @ +20°C ambient		-110°C with +/-0.05°C thermo stating precision	
Dark Current @ -110°C		1 e-/p/hr	
Nonlinearity		<2%	
Readout bits/speed		16 bits @ 1 MHz; 16 bits @ 100 kHz	
Frame readout		4.5 seconds for full frame @ 1 MHz 41 seconds for full frame @ 100kHz	
LN hold time		24 hours	
Operating environment		0 to 30°C ambient, 0 to 50% relative humidity noncondensing	

*based on CCD manufacturer's cosmetic blemish definitions
All specifications subject to change without notice

Quantum Efficiency Curve

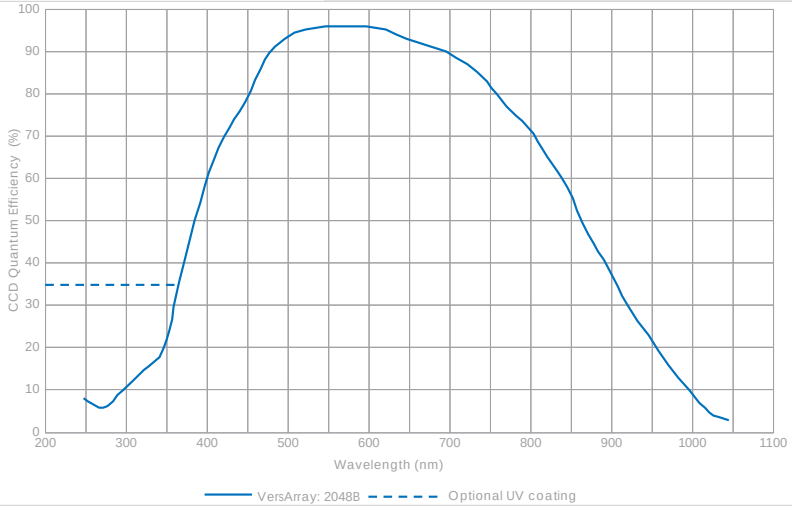

Princeton Instruments

www.piacton.com
email: moreinfo@piacton.com
USA +1.877.4 PIACTON | Benelux +31 (347) 324989
France +33 (1) 60.86.03.65 | Germany +49 (0) 89.660.779.3
UK +44 (0) 28.38310171 | Asia/Pacific +65.6293.3130
China +86 135 0122 8135 | Japan +81.3.5639.2741

C Scripts for RV measurement

```
#==========================================================================
# Creates files with lists of bias, dark, flat, thar and scientific frames
#==========================================================================

path_wd=/home/marie/giants_data/Ondrejov/20200709/ # path to the directory with frames (folders comp,
 flat, zero, object, etc.)
# object=TOI1143-01   # Object of interest (frames placed in the object folder)

mkdir $path_wd'working_dir'

# object
# ls $path_wd'object/'$object > $path_wd'working_dir/'obj.list
# cp $path_wd'object/'$object'/'*.fit $path_wd'working_dir/'
ls $path_wd'object/' > $path_wd'/'ls_temp
for f in $(cat ls_temp ); do
    cp $path_wd'object/'$f'/'*.fit $path_wd'working_dir/'
done
rm ls_temp
ls $path_wd'working_dir/' | grep -v '.list' > $path_wd'working_dir/'obj.list

# zero frames - creation of bias list and copying frames into working_dir folder
ls $path_wd'zero' > $path_wd'working_dir/'bias.list
cp $path_wd'zero/'*.fit $path_wd'working_dir/'

# flaty
ls $path_wd'flat' > $path_wd'working_dir/'flat.list
cp $path_wd'flat/'*.fit $path_wd'working_dir/'

# comp
ls $path_wd'comp' > $path_wd'working_dir/'comp.list
cp $path_wd'comp/'*.fit $path_wd'working_dir/'

cat $path_wd'working_dir/'bias.list $path_wd'working_dir/'flat.list $path_wd'working_dir/'obj.list $path_wd'
working_dir/'comp.list > $path_wd'working_dir/'All_frames.list

cat $path_wd'working_dir/'bias.list $path_wd'working_dir/'flat.list $path_wd'working_dir/'obj.list > $path_w
d'working_dir/'frames.list

# Creation of lists with default names in particular steps
awk '{print "b_"($1)}' $path_wd'working_dir/'flat.list > $path_wd'working_dir/'b_flat.list
awk '{print "bf_"($1)}' $path_wd'working_dir/'obj.list > $path_wd'working_dir/'bf_obj.list
awk '{print "bf_"($1)}' $path_wd'working_dir/'comp.list > $path_wd'working_dir/'bf_comp.list

sed -e 's/\./.ec./' $path_wd'working_dir/'bf_obj.list | sed -e 's/$/s/' > $path_wd'working_dir/'obj.ec.list
sed -e 's/\.ec./.ecd./' $path_wd'working_dir/'obj.ec.list > $path_wd'working_dir/'obj.ecd.list

sed -e 's/\.ecd\./\.cont\./g' $path_wd'working_dir/'obj.ecd.list > $path_wd'working_dir/'cont.list
sed -e 's/\.ecd\./\.normf\./g' $path_wd'working_dir/'obj.ecd.list > $path_wd'working_dir/'normf.list
sed -e 's/\.ecd\./\.ec1d\./g' $path_wd'working_dir/'obj.ecd.list > $path_wd'working_dir/'ec1d.list
sed -e 's/\.ecd\./\.normf1d\./g' $path_wd'working_dir/'obj.ecd.list > $path_wd'working_dir/'normf1d.list
sed -e 's/\.ecd\./\.cont1d\./g' $path_wd'working_dir/'obj.ecd.list > $path_wd'working_dir/'cont1d.list
sed -e 's/\.cont1d.fits/\.dat/g' $path_wd'working_dir/'cont1d.list > $path_wd'working_dir/'txt.list

# Copying of scripts into the working directory
cp -R /home/marie/giants_data/Ondrejov/data_reduction/from_Marek/Spectra/* $path_wd'working_dir' # p
```

```
lease change the path to the folder where the scripts and templates are stored (default /home/$user/Spec
tra/)

# ================= Cosmic remove using dcr ==============================
# Removes cosmics in all frames except for the ThAr frames
# ======================================================================
for f in $(cat working_dir/frames.list); do
echo '========================= '$f' ========================='
	/home/marie/giants_data/Ondrejov/dcr/./dcr working_dir/$f working_dir/$f working_dir/cosmics_log.tx
t
done
```

```
# ==============================================================================
==============================================
# Bad-pixel correction, cosmic removal, trimming of the frames, making of the master bias (mbias) and m
aster flat frames (mflat)
# ==============================================================================
==============================================

fixpix images=@All_frames.list masks=badpixmask    # bad-pixel correction
noao
imred
crutil        # load of the package containing task cosmicrays
cosmicrays input=@frames.list output=@frames.list   # cosmics removal
bye
imcopy *fit[5:2039,500:1749] *fit     # trim of the frames
#imcopy Aper_Template.fits[5:2039,500:1749] Aper_Template.fits
ccdred
zerocombine input=@bias.list output=mbias    # making of the master bias
imarith operand1=@flat.list op=- operand2=mbias result=@b_flat.list # subtraction of bias from flat field fr
ames
flatcombine input=@b_flat.list output=mflat    # making of the master flat

# ============================
# making of the normalized flat
# ============================
bye
bye
twodspec
apextract

apall input=Aper_Template output=Aper_Template format=echelle referen="" interac=yes find=yes recent
e=yes resize=no edit=yes trace=yes fittrace=yes extract=no extras=no review=no lower=-4.0 upper=4.0 t
_nsum=10 t_step=5 t_nlost=3 t_funct=legendre t_order=3 t_sampl=* t_niter=5 t_low_r=3 t_high_r=3 back
gro=none

apflatten input=mflat output=nflat referen=Aper_Template interac=yes find=no recente=yes resize=no edit
=yes trace=no fittrace=no flatten=yes fitspec=yes

# ====================================
# mbias subtraction, division by nflat
# ====================================
imarith operand1=@comp.list op=- operand2=mbias result=@bf_comp.list
imarith operand1=@bf_comp.list op=/ operand2=nflat result=@bf_comp.list
imarith operand1=@obj.list op=- operand2=mbias result=@bf_obj.list
imarith operand1=@bf_obj.list op=/ operand2=nflat result=@bf_obj.list

# ==============================================
# extraction of the apertures (scientific frames)
# ==============================================
apall input=@bf_obj.list output="" format=echelle referen=Aper_Template interac=no find=no recente=yes
 resize=no edit=yes trace=no fittrace=no extract=yes extras=no review=no lower=-4.0 upper=4.0
```

```
# ======================================
# Extracts spectra from the ThAr frames.

# !!!!! The input file is the last ThAr in the night, output is the number of the scientific frame the comp spect
rum #refers to. This needs to be modified.
#input: the last ThAr frame
#output: XXcomp.ec (xx means the number of the scientific frame)
#referen: the scientific frame

#The number of rows below must be the same as is the number of the scientific frames!!!!!

# ======================================

reset imtype = fits

noao
twodspec
apextract

apall input=bf_e202007090030 output=31comp.ec referen=bf_e202007090031 interac=no find=no recent
e=no resize=no edit=no trace=no fittrace=no extract=yes extras=no review=no lower=-4. upper=4.
apall input=bf_e202007090030 output=32comp.ec referen=bf_e202007090032 interac=no find=no recent
e=no resize=no edit=no trace=no fittrace=no extract=yes extras=no review=no lower=-4. upper=4.
apall input=bf_e202007090030 output=33comp.ec referen=bf_e202007090033 interac=no find=no recent
e=no resize=no edit=no trace=no fittrace=no extract=yes extras=no review=no lower=-4. upper=4.
apall input=bf_e202007090030 output=34comp.ec referen=bf_e202007090034 interac=no find=no recent
e=no resize=no edit=no trace=no fittrace=no extract=yes extras=no review=no lower=-4. upper=4.
apall input=bf_e202007090030 output=35comp.ec referen=bf_e202007090035 interac=no find=no recent
e=no resize=no edit=no trace=no fittrace=no extract=yes extras=no review=no lower=-4. upper=4.
apall input=bf_e202007090030 output=36comp.ec referen=bf_e202007090036 interac=no find=no recent
e=no resize=no edit=no trace=no fittrace=no extract=yes extras=no review=no lower=-4. upper=4.
apall input=bf_e202007090030 output=37comp.ec referen=bf_e202007090037 interac=no find=no recent
e=no resize=no edit=no trace=no fittrace=no extract=yes extras=no review=no lower=-4. upper=4.
apall input=bf_e202007090041 output=38comp.ec referen=bf_e202007090038 interac=no find=no recent
e=no resize=no edit=no trace=no fittrace=no extract=yes extras=no review=no lower=-4. upper=4.
apall input=bf_e202007090041 output=39comp.ec referen=bf_e202007090039 interac=no find=no recent
e=no resize=no edit=no trace=no fittrace=no extract=yes extras=no review=no lower=-4. upper=4.
apall input=bf_e202007090041 output=40comp.ec referen=bf_e202007090040 interac=no find=no recent
e=no resize=no edit=no trace=no fittrace=no extract=yes extras=no review=no lower=-4. upper=4.

ls [0-9]*comp.ec.fits | sort -n > comp.ec.list

bye
bye
bye
```

```
noao
imred
echelle


# ====== ecreidentification ========
ecreidentify images=@comp.ec.list referenc=ThAr_Template refit=yes

# ====== refspectra ================
refspectra input=@obj.ec.list referen=@comp.ec.list override=yes

# ======== dispcor =================
dispcor input=@obj.ec.list output=@obj.ecd.list

# ======== continuum fitting ========
continuum input=@obj.ecd.list output=@cont.list type=ratio interac=no naverag=10 functio=spline3 order
=5 low_rej=2 high_rej=5 niterat=10

# ======== merging the orders to 1-d spectrum ==============
sarith @obj.ecd.list / @cont.list @normf.list
scombine @obj.ecd.list output=@ec1d.list group=images combine=sum
scombine @normf.list output=@normf1d.list group=images combine=sum
sarith @ec1d.list / @normf1d.list @cont1d.list

imreplace @cont1d.list value=1 lower=0 upper=0.0001
```

References

ÅNGSTRÖM, A. J. Optiska undersökningar. 1853. In Swedish.

BALL, W.W.Rouse. A short account of the history of mathematics. New York: Dover, 1908. ISBN 978-0-486-20630-1.

BENNETT, G. G. The Calculation of Astronomical Refraction in Marine Navigation. Journal of Navigation. 1982, 35(2), 255-259. ISSN 0373-4633. Available from: https://doi.org/10.1017/S0373463300022037

BOHR, N. XXXVII. On the constitution of atoms and molecules. The London, Edinburgh, and Dublin Philosophical Magazine and Journal of Science. 1913, 26(153), 476-502. ISSN 1941-5982. Available from: https://doi.org/doi:10.1080/14786441308634993

BRAND, John C. D. Lines of Light: The Sources of Dispersive Spectroscopy, 1800 - 1930. Gordon and Breach Publishers, 1995. ISBN 978-2884491624.

BUNSEN, R. a G. KIRCHHOFF. Untersuchungen über das Sonnenspektrum und die Spektren der Chemischen Elemente. 1861.

BURGESS, C. a K.D. MIELENZ. Advances in Standards and Methodology in Spectrophotometry. Burlington: Elsevier Science, 1987, 416 p. ISBN 9780444599056.

EDEN, A. The Search For Christian Doppler. Wien: Springer-verlag, 1992. ISBN 978-0-387-82367-6.

EINSTEIN, A. Über einen die Erzeugung und Verwandlung des Lichtes betreffenden heuristischen Gesichtspunkt. Annalen der Physik. 1905, 322(6), 132-148. ISSN 00033804. Available from: https://doi.org/10.1002/andp.19053220607

FRAUNHOFER, Joseph. Bestimmung des Brechungs- und des Farben-Zerstreuungs - Vermögens verschiedener Glasarten, in Bezug auf die Vervollkommung achromatischer Fernröhre: Denkschriften der Königlichen Akademie der Wissenschaften zu München. 5. 1815.

Gaia Collaboration, Vallenari, A., Brown, A. G. A., et al. 2022, arXiv:2208.00211. Available from: https://doi.org/10.48550/arXiv.2208.00211

GUSTAFSSON, B. 1992, European Southern Observatory Conference and Workshop Proceedings, 40, 17

HERTZ, H. Ueber einen Einfluss des ultravioletten Lichtes auf die electrische Entladung. Annalen der Physik und Chemie. 1887, 267(8), 983-1000. ISSN 00033804. Available from: https://doi.org/10.1002/andp.18872670827

HOCKBERGER, Philip E. A History of Ultraviolet Photobiology for Humans,Animals and Microorganisms. Photochemistry and Photobiolog. Department of Physiology, The Feinberg School of Medicine, Northwestern University, Chicago, IL: Elsevier, 2002, 76(6), 561-579. ISSN 0031-8655. Available from: https://doi.org/10.1562/0031-8655(2002)0760561AHOUPF2.0.CO2

HOUDAS, Y. Doppler, Buys-Ballot, Fizeau. Historical note on the discovery of the Doppler's effect. Annales de cardiologie et d'angéiologie. 1991, 40(4), 209-13. 2053764.

KALER, James B. Stars and their Spectra: An Introduction to the Spectral Sequence. Second edition. New York: Cambridge University Press, 2011. ISBN 978-0-521-89954-3.

KABÁTH, P., M. SKARKA, S. SABOTTA, et al. Ondřejov Echelle Spectrograph, Ground Based Support Facility for Exoplanet Missions. Publications of the Astronomical Society of the Pacific. 2020, 132(1009). ISSN 0004-6280. Available from: https://doi.org/10.1088/1538-3873/ab6752

KOUBSKÝ, P., MAYER, P., ČÁP, J., et al. 2004, Publications of the Astronomical Institute of the Czechoslovak Academy of Sciences, 92, 37

MASSEY, P. & JACOBY, G. H. 1992, Astronomical CCD Observing and Reduction Techniques, 23, 240

MILLIKAN, R. A. A Direct Determination of " h .." Physical Review. 1914, 4(1), 73-75. ISSN 0031-899X. Available from: https://doi.org/10.1103/PhysRev.4.73.2

NOVELLINE, Robert A. Squire's fundamentals of radiology. 5th ed. Cambridge: Harvard University Press, 1997. ISBN 06-740-1279-8.

PALMA, Christopher. Kirchoff's Laws and Spectroscopy. Astro 801 [online]. Department of Astronomy and Astrophysics, The Pennsylvania State University [cit. 2023-05-07]. Available from: https://www.e-education.psu.edu/astro801/content/l3_p6.html

SIMBAD Astronomical Database [online]. [cit. 2023-04-28]. Available from: http://simbad.cds.unistra.fr/simbad/

ŠLECHTA, Miroslav. Modernizace 2m Perkova dalekohledu v Ondřejově. Astropis. 2020, XXVII(123-2020), 12-15. ISSN 1211-0485.

ŠLECHTA, Miroslav. OES [e-mail]. Message from: miroslav.slechta@asu.cas.cz, Message to: 500050@muni.cz 17. 5. 2023 12:22 [cit. 17. 5. 2023].

ŠLECHTA, Miroslav. vlákno do OESu [e-mail]. Message from: miroslav.slechta@asu.cas.cz, Message to: 500050@muni.cz 17. 5. 2023 16:32 [cit. 17. 5. 2023].

ŠLECHTA, Miroslav. Dotazy k echelletovému spektrografu a modernizaci roku 2019 [e-mail]. Message from: miroslav.slechta@asu.cas.cz, Message to: 500050@muni.cz 10. 5. 2023 15:48 [cit. 10. 5. 2023].

ŠLECHTA, Miroslav. Prosba o fotografie z modernizace Perkova dalekohledu [e-mail]. Message from: miroslav.slechta@asu.cas.cz, Message to: 500050@muni.cz 24. 4. 2023 15:32, 25. 04. 2023 0:29 [cit. 26. 4. 2023].

ŠTEGNER, David. *Vzorová spektra hvězd hlavní posloupnosti pro Ondřejovský Echelletový Spektrograf* [online]. Brno, 2020 [cit. 2023-05-16]. Available from: https://is.muni.cz/th/sg0k5/. Bachelor thesis. Masaryk University, Faculty of Science. Supervisor Marek SKARKA.

TALBOT, H.F., Some experiments on coloured flames. In: TALBOT, H.F. The Edinburgh Journal of Science, 1826.

TRNKA, Michal. Dalekohled v Ondřejově nese jméno astronoma Perka. In: Český rozhlas Region [online]. 2012, 7. 8. 2012 [cit. 2023-04-16]. Available from: https://region.rozhlas.cz/dalekohled-v-ondrejove-nese-jmeno-astronoma-perka-7266220

WEEKS, Mary Elvira. Discovery Of The Element. 6th edition. Journal Of Chemical Education, 1956.

WILLIAMS, R. a G. WILLIAMS. PIONEERS OF INVISIBLE RADIATION PHOTOGRAPHY. Medical and Scientific Photography: An online resource for doctors, scintists and students [online]. 2002 [cit. 2023-05-06]. Available from: https://medicalphotography.com.au/Article_04/03.html

WOLLASTON, William Hyde. A method of examining refractive and dispersive powers, by prismatic reflection. Philosophical Transactions of the Royal Society of London. 1802. Available from: https://doi.org/10.1098/rstl.1802.0014

YOUNG, Andrew T. a William M. IRVINE. Multicolor photoelectric photometry of the brighter planets. I. Program and Procedure. The Astronomical Journal. 1967, 72, 945-950. ISSN 00046256. Available from: https://doi.org/10.1086/110366
electronic sources

Stelar kinematics. In: Wikipedia: the free encyclopedia [online]. San Francisco (CA): Wikimedia Foundation, 2023 [cit. 2023-04-25]. Available from: https://en.wikipedia.org/wiki/Stellar_kinematics

The Era of Classical Spectroscopy. In: MIT Spectroscopy [online]. [cit. 2023-05-06]. Available from: http://web.mit.edu/spectroscopy/history/history-classical.html

OPENSTAX ASTRONOMY. Spectroscopy in Astronomy. OpenStax CNX [online]. 2016 [cit. 2023-05-06]. Available from: https://openstax.org/books/astronomy-2e/pages/5-3-spectroscopy-in-astronomy

Identifying Elements in the Sun Using Spectral Lines [online]. [cit. 2023-04-25]. Available from: http://www.columbia.edu/~vjd1/Solar%20Spectrum%20Ex.html

The Discovery of Radioactivity. Guide to the Nuclear Wall Chart [online]. 2000 [cit. 2023-05-08]. Available from: https://www2.lbl.gov/abc/wallchart/chapters/03/4.html

The Nobel Prize in Physics 1921. Nobelprize.org [online]. [cit. 2023-05-08]. Available from: https://www.nobelprize.org/nobel_prizes/physics/laureates/1921/

Bohr model. In: Wikipedia: the free encyclopedia [online]. San Francisco (CA): Wikimedia Foundation, 2023 [cit. 2023-05-08]. Available from: https://en.wikipedia.org/wiki/Bohr_model

Professor Buys Ballot investigates the Doppler Effect. Utrecht University [online]. [cit. 2023-05-09]. Available from: https://muurformules.sites.uu.nl/mural-paintings/christophorus-buys-ballot/?lang=en

Doppler effect. In: Wikipedia: the free encyclopedia [online]. San Francisco (CA): Wikimedia Foundation, 2023 [cit. 2023-05-10]. Available from: https://en.wikipedia.org/wiki/Doppler_effect

Signal-to-Noise Ratio. SHIMADZU CORPORATION [online]. [cit. 2023-04-25]. Available from: https://www.shimadzu.com/an/service-support/technical-support/gas-chromatograph-mass-spectrometry/analysis-results/signal/definition.html

Perkův 2-m dalekohled. Stelární oddělení [online]. [cit. 2023-04-25]. Available from: https://stelweb.asu.cas.cz/cs/perkuv-dalekohled/

Ondřejov. In: Wikipedia: the free encyclopedia [online]. San Francisco (CA): Wikimedia Foundation, 2023 [cit. 2023-05-11]. Available from: https://cs.wikipedia.org/wiki/Ond%C5%99ejov

Specifikace Perkova dalekohledu [online]. [cit. 2023-04-16]. Available from: https://stelweb.asu.cas.cz/cs/perkuv-dalekohled/specifikace-dalekohledu/

Pecný (Benešovská pahorkatina). In: Wikipedia: the free encyclopedia [online]. San Francisco (CA): Wikimedia Foundation, 2023 [cit. 2023-05-11]. Available from: https://cs.wikipedia.org/wiki/Pecn%C3%BD_(Bene%C5%A1ovsk%C3%A1_pahorkatina)

Echelle spectrograph. Stelar Physics Department [online]. [cit. 2023-05-10]. Available from: https://stelweb.asu.cas.cz/en/telescope/instrumentation/oes-spectrograph/

Optra UV, Optra WF: Silica/silica fiber with optional buffers. CeramOptec [online]. [cit. 2023-05-17]. Available from: https://www.ceramoptec.com/fileadmin/user_upload/pdf/pdf_data_sheets_neu_Sept2016/ceramoptec_EN_Optran_UV_WF.pdf

Princeton Instruments VersArray:2048B. OBSERVATORIO DE SIERRA NEVADA, IAA-CSIC [online]. [cit. 2023-05-19]. Available from: https://www.osn.iaa.csic.es/sites/default/files/documents/versarray2048b_ccdt90.pdf